



Publication Year	2016
Acceptance in OA@INAF	2020-05-13T12:10:39Z
Title	Hi-GAL, the Herschel infrared Galactic Plane Survey: photometric maps and compact source catalogues. First data release for the -70°
Authors	MOLINARI, Sergio; SCHISANO, EUGENIO; ELIA, Davide Quintino; Pestalozzi, M.; TRAFICANTE, ALESSIO; et al.
DOI	10.1051/0004-6361/201526380
Handle	http://hdl.handle.net/20.500.12386/24790
Journal	ASTRONOMY & ASTROPHYSICS
Number	591

Hi-GAL, the *Herschel* infrared Galactic Plane Survey: photometric maps and compact source catalogues

First data release for the inner Milky Way: $+68^\circ \geq l \geq -70^\circ$ ★,★★

S. Molinari¹, E. Schisano¹, D. Elia¹, M. Pestalozzi¹, A. Traficante², S. Pezzuto¹, B. M. Swinyard³,
 A. Noriega-Crespo⁴, J. Bally⁵, T. J. T. Moore⁶, R. Plume⁷, A. Zavagno⁸, A. M. di Giorgio¹, S. J. Liu¹, G. L. Pilbratt⁹,
 J. C. Mottram¹⁰, D. Russeil⁸, L. Piazzo¹¹, M. Veneziani¹², M. Benedettini¹, L. Calzoletti^{13,14}, F. Faustini¹⁴, P. Natoli¹⁵,
 F. Piacentini¹⁶, M. Merello¹, A. Palmese¹, R. Del Grande¹, D. Polychroni¹⁷, K. L. J. Rygl¹⁸, G. Polenta¹⁴,
 M. J. Barlow¹⁹, J.-P. Bernard^{20,21}, P. G. Martin²², L. Testi^{23,24}, B. Ali²⁵, P. André²⁶, M. T. Beltrán²⁴, N. Billot²⁷,
 S. Carey²⁸, R. Cesaroni²⁴, M. Compiègne²⁹, D. Eden³⁰, Y. Fukui³¹, P. Garcia-Lario¹³, M. G. Hoare³², M. Huang³³,
 G. Joncas³⁴, T. L. Lim^{3,13}, S. D. Lord³⁵, S. Martinavarro-Armengol¹⁹, F. Motte²⁶, R. Paladini¹², D. Paradis^{20,21},
 N. Peretto³⁶, T. Robitaille³⁷, P. Schilke³⁸, N. Schneider³⁹, B. Schulz¹², B. Sibthorpe⁴⁰, F. Strafella⁴¹,
 M. A. Thompson⁴², G. Umana⁴³, D. Ward-Thompson⁴⁴, and F. Wyrowski⁴⁵

(Affiliations can be found after the references)

Received 22 April 2015 / Accepted 10 February 2016

ABSTRACT

Aims. We present the first public release of high-quality data products (DR1) from Hi-GAL, the *Herschel* infrared Galactic Plane Survey. Hi-GAL is the keystone of a suite of continuum Galactic plane surveys from the near-IR to the radio and covers five wavebands at 70, 160, 250, 350 and 500 μm , encompassing the peak of the spectral energy distribution of cold dust for $8 \lesssim T \lesssim 50$ K. This first Hi-GAL data release covers the inner Milky Way in the longitude range $68^\circ \geq l \geq -70^\circ$ in a $|b| \leq 1^\circ$ latitude strip.

Methods. Photometric maps have been produced with the ROMAGAL pipeline, which optimally capitalizes on the excellent sensitivity and stability of the bolometer arrays of the *Herschel* PACS and SPIRE photometric cameras. It delivers images of exquisite quality and dynamical range, absolutely calibrated with *Planck* and IRAS, and recovers extended emission at all wavelengths and all spatial scales, from the point-spread function to the size of an entire $2^\circ \times 2^\circ$ “tile” that is the unit observing block of the survey. The compact source catalogues were generated with the CuTex algorithm, which was specifically developed to optimise source detection and extraction in the extreme conditions of intense and spatially varying background that are found in the Galactic plane in the thermal infrared.

Results. Hi-GAL DR1 images are cirrus noise limited and reach the 1σ -rms predicted by the *Herschel* Time Estimators for parallel-mode observations at $60'' \text{ s}^{-1}$ scanning speed in relatively low cirrus emission regions. Hi-GAL DR1 images will be accessible through a dedicated web-based image cutout service. The DR1 Compact Source Catalogues are delivered as single-band photometric lists containing, in addition to source position, peak, and integrated flux and source sizes, a variety of parameters useful to assess the quality and reliability of the extracted sources. Caveats and hints to help in this assessment are provided. Flux completeness limits in all bands are determined from extensive synthetic source experiments and greatly depend on the specific line of sight along the Galactic plane because the background strongly varies as a function of Galactic longitude. Hi-GAL DR1 catalogues contain 123210, 308509, 280685, 160972, and 85460 compact sources in the five bands.

Key words. dust, extinction – infrared: ISM – stars: formation – Galaxy: disk – methods: data analysis – techniques: photometric

1. Introduction

The Milky Way Galaxy, our home, is a complex ecosystem in which a cyclical transformation process brings diffuse baryonic matter into dense, unstable condensations to form stars. The stars produce radiant energy for billions of years before releasing chemically enriched material back into the interstellar medium (ISM) in their final stages of evolution.

Although considerable progress has been made in the past two decades in understanding the evolution of isolated dense

molecular clumps toward the onset of gravitational collapse and the formation of stars and planetary systems, much remains hidden. We do not know the relative importance of gravity, turbulence, or the perturbation from spiral arms in assembling the diffuse and mostly atomic Galactic ISM into dense, molecular, filamentary structures and compact clumps. We do not know how turbulence, gravity, and magnetic fields interact on different spatial scales to bring a diffuse cloud on the verge of star formation. We still do not have a comprehensive quantitative understanding of the relative importance of external triggers in the process, although available evidence suggests that triggering is not a major pathway for star formation (Thompson et al. 2012; Kendrew et al. 2012). We do not know how the relative roles played by these different agents changes from extreme environments like the Galactic centre to the quiet neighbourhoods of the Galaxy beyond the solar circle.

* *Herschel* is an ESA space observatory with science instruments provided by European-led Principal Investigator consortia and with important participation from NASA.

** The images and the catalogues are only available at the CDS via anonymous ftp to cdsarc.u-strasbg.fr (130.79.128.5) or via <http://cdsarc.u-strasbg.fr/viz-bin/qcat?J/A+A/591/A149>

Today, it is possible for the first time to engage with this ambitious challenge, thanks to a new suite of modern Milky Way surveys that provide homogenous coverage of the entire Galactic plane (hereafter GP) and that have already started to transform the view of our Galaxy as a global star-formation engine (see [Molinari et al. 2014](#) for a recent review).

The UKIDSS Galactic Plane Survey ([Lucas et al. 2008](#)) on the 4m UK Infrared Telescope on Hawaii covered the three near-IR photometric bands (J , H and K) to eighteenth magnitude, producing catalogues of over a billion stars. The unprecedented depth (fifteenth mag) and resolution ($2''$) of the NASA *Spitzer* satellite's GLIMPSE survey was the first to deliver a new global view of the Galaxy at wavelengths of 3.6, 4.5, 5.8, and $8.0\ \mu\text{m}$ ([Benjamin et al. 2005](#)), until then only partially accessible from the ground and with imaging capabilities limited to resolutions of a few arcminutes, at best. The resulting catalogue of 49 million sources is dominated by stars and, to a lesser extent, by pre-main-sequence young stellar objects (YSOs), with the $8.0\text{-}\mu\text{m}$ channel also showing strong extended emission that probes the interaction between the UV radiation from hot stars and molecular clouds. The *Spitzer*-MIPSGAL survey at $24\ \mu\text{m}$ ([Carey et al. 2009](#)) enables much deeper penetration of the dense molecular clouds to reveal nascent intermediate and high-mass stars. These surveys were limited to the inner third of the Milky Way GP and were complemented by GLIMPSE360, which used *Spitzer* in its warm mission to complete the coverage of the entire GP at 3.6 and $4.5\ \mu\text{m}$, and by the *WISE* satellite ([Wright et al. 2010](#)), which, as part of its all-sky survey, is covering the entire GP (although at lower resolution than *Spitzer*) between 3 and $25\ \mu\text{m}$.

At far-infrared and millimetre wavelengths, AKARI surveyed the entire sky between $65\ \mu\text{m}$ and $160\ \mu\text{m}$ in 2006–2007. Its spatial resolution of between $1'$ and $1'.5$ ([Doi et al. 2016](#)) represented an improvement by a factor ~ 3 over that of IRAS, although still a factor ~ 5 larger than *Herschel*. The *Planck* satellite ([Planck Collaboration I 2011](#)) also surveyed the entire sky at wavelengths between $350\ \mu\text{m}$ and 1cm , but with a resolution $>5'$, which is insufficient to resolve the complexity of the thermal dust emission in star-forming clouds.

Only ground-based facilities can at the moment achieve resolutions below $1'$ in the millimetre regime. The ATLASGAL survey ([Schuller et al. 2009](#)) has used the 12 m APEX telescope in Chile to map the portion of the GP at longitudes between roughly $+60^\circ$ and -60° at $870\ \mu\text{m}$, the JPS survey ([Moore et al. 2015](#)), using the JCMT antenna in Hawaii, gives deeper coverage at somewhat higher resolution in the northern part of this same region at $850\ \mu\text{m}$, while the Bolocam GPS covers the first quadrant at 1.1 mm ([Aguirre et al. 2011](#)). These (sub-)millimetre surveys provide a census of the cold and compact dust condensations that harbour star-formation; mass estimates require assumptions about dust temperatures that the single-band survey data themselves cannot constrain, however.

Radio-wavelength continuum observations provide extinction-free views of bremsstrahlung radiation from ultra-compact HII (UCHII) regions and the ionised ISM in general. The $1'.5$ resolution, 6 cm CORNISH survey used the Very Large Array telescope to map the $\ell = +10^\circ$ to $+65^\circ$ section of the GP at resolutions of $\sim 1''$ to $\sim 10''$ ([Purcell et al. 2013](#)). The CORNISH-South extension of the project, carried out with the ATCA array, will complement this information for the corresponding region of the fourth quadrant, augmented with imaging in radio recombination lines.

This suite of continuum GP surveys is ideally complemented by a family of spectroscopic surveys of molecular and atomic emission lines. Kinematic information on the same dense clouds

traced by the thermal emission from cool dust can also be traced using molecular-line emission. The Galactic Ring Survey (GRS; [Jackson et al. 2006](#)), at $46''$ resolution, uses the FCRAO 14 m antenna to map the ^{13}CO ($J = 1-0$) transition in the range $15^\circ \lesssim \ell \lesssim 56^\circ$. The JCMT COHRS survey ([Dempsey et al. 2013](#)) covers essentially the same longitude range as the GRS, but in the CO ($J = 3-2$) line and at a spatial resolution of $14''$.

Additional extensions to the GRS, in the first and second quadrants, toward the Galactic anticentre, also in ^{12}CO ($J = 1-0$), have been carried out with the FCRAO ([Heyer et al. 1998](#); Brunt et al., in prep.). The International Galactic Plane Survey (IGPS) has combined three interferometric 21 cm HI surveys at $45\text{--}60''$ resolution. This combination provides an ideal tool to study the transformation of atomic into molecular gas in the spiral arms (e.g. [McClure-Griffiths et al. 2001](#)).

The coverage of the third and fourth quadrants in molecular lines is more sparse and less systematic. Together with targeted-source line surveys like MALT90 ([Jackson et al. 2013](#)), unbiased coverage of the plane is limited to the NANTEN survey (e.g. [Mizuno & Fukui 2004](#)), which is currently being improved with the NANTEN2/NASCO project, which still has limited ($\sim 4'$) spatial resolution, however. Recent unbiased surveys with the Mopra antenna in Australia ([Burton et al. 2013](#); [Jones et al. 2012](#)) are starting to fill the gap with the data quality of the CO surveys in the northern portion of the GP. The SEDIGISM survey is currently being executed to map the fourth quadrant between $\ell = +18^\circ$ and $\ell = -60^\circ$ in ^{13}CO and C^{18}O ($J = 2-1$) with the APEX telescope.

The Methanol Multi-Beam survey (e.g. [Green et al. 2012](#)) is searching the plane for 6.7 GHz methanol maser emission using the Parkes and ATCA telescopes. Methanol maser emission is characteristic of the early formation stage of massive stars; its association with cool dense clumps is a signpost for ongoing formation of massive stars and associated protoclusters in such objects. A more complete compilation of GP Surveys from the near-IR to the radio is provided in the review of [Molinari et al. \(2014\)](#).

The *Herschel* infrared Galactic Plane Survey (Hi-GAL, [Molinari et al. 2010b,a](#)), carried out with the *Herschel* Space Observatory ([Pilbratt et al. 2010](#)), is the keystone in the arch of GP continuum surveys. With a full plane coverage of the thermal far-IR and submillimetre continuum in five bands between $70\ \mu\text{m}$ and $500\ \mu\text{m}$, ideally covering the peak of the spectral energy distribution (SED) of dust in the temperature range $8\text{ K} \leq T \leq 50\text{ K}$, Hi-GAL delivers a complete census of structures containing cold dust, from the central molecular zone to the outskirts of the Galaxy, enabling self-consistent determination of dust temperatures and masses. Thanks to its space-borne platform, the *Herschel* cameras do not suffer from the rapid atmospheric variabilities that limit ground-based submillimetre facilities. This allows full exploitation of the excellent sensitivity and stability of the infrared bolometric arrays to deliver exquisite-quality images that recover extended emission from dust on all spatial scales. The ability of *Herschel* to recover multi-wavelength extended emission from the diffuse ISM, through dense filamentary structures, down to compact and point-like sources ([Molinari et al. 2010a](#); [André et al. 2010](#)) are and will remain unparalleled in the coming decades.

Hi-GAL is delivering a transformational view of the complete evolutionary path that brings cold and diffuse interstellar material to condense into clouds and filaments that then fragment into protocluster-forming dense clumps. More than 50 papers have been published by the Hi-GAL consortium to date, based on Hi-GAL images and preliminary source catalogues, from

studies of the diffuse ISM (e.g. Bernard et al. 2010; Paradis et al. 2010; Compiègne et al. 2010; Traficante et al. 2014; Elia et al. 2014) to dense, large-scale filaments (Molinari et al. 2010a; Schisano et al. 2014; Wang et al. 2015), dust in HII regions (e.g. Paladini et al. 2012; Tibbs et al. 2012), clumps and massive star formation (e.g. Elia et al. 2010, 2013; Bally et al. 2010; Battersby et al. 2011; Mottram & Brunt 2012; Wilcock et al. 2012; Veneziani et al. 2013; Beltrán et al. 2013; Strafella et al. 2015; Traficante et al. 2015), Galactic central molecular zone studies (Molinari et al. 2011a; Longmore et al. 2012), triggered star formation (Zavagno et al. 2010), and finally dust around post-main-sequence objects (Umana et al. 2012; Martinavarró-Armengol et al., in prep.). More papers are in preparation by the Hi-GAL Consortium. Although basic Hi-GAL data have always been open for public access through the *Herschel* Science Archive, we are now providing access for the larger community to the high-quality data products (maps and source catalogs) used internally by the Hi-GAL consortium.

In this paper we present the first public release of Hi-GAL data products (DR1). DR1 is limited to the inner Milky Way in the longitude range $+68^\circ \geq \ell \geq -70^\circ$ and latitude range $1^\circ \geq b \geq -1^\circ$, and consists of calibrated and astrometrically registered images at 70, 160, 250, 350, and 500 μm , plus compact-source catalogues, delivered via an image cutout service provided by the ASI Science Data Center¹. We present and discuss the production methods and characterisation of the images and catalogues considered according to their band-specific properties. A full systematic analysis of the physical properties of dense, star-forming and potentially star-forming condensations (reconstructed from the band-merged Hi-GAL photometric catalogues with augmented SED coverage from ancillary surveys from the mid-IR to the millimetre) will be presented in Elia et al., (in prep.). A first systematic analysis of far-IR properties of post-main-sequence objects based on the Hi-GAL catalogues is presented in Martinavarró-Armengol et al. (in prep.).

2. Observations

The motivations and observing strategy adopted for the Hi-GAL Survey are described in detail in Molinari et al. (2010b). The complete survey was assembled in three instalments of observing time granted in open time competition in each of the three calls issued during the *Herschel* project lifetime. Because of a clerical inconsistency in determining the duration time of the observations, a longitude range of about 6° in extent in the outer Galaxy could not be executed in the observing time formally granted for the complete plane coverage, and director's discretionary time was additionally granted to obtain the 360° -wide coverage. The total observing time amounted to slightly more than 900 h, making the full Hi-GAL survey the largest observing program carried out by *Herschel*.

The Hi-GAL observations were acquired by subdividing the surveyed area into square tiles of $\sim 2^\circ \times 2^\circ$ in size, to obtain complete coverage of a $|b| \leq 1^\circ$ strip of the Galactic plane at 70, 160, 250, 350, and 500 μm simultaneously. Each tile was observed with the PACS (Poglitsch et al. 2010) and SPIRE (Griffin et al. 2010) cameras in parallel mode (pMode), specifically designed to optimise data acquisition for large-area multi-wavelength surveys. In pMode the PACS and SPIRE cameras are used simultaneously, effectively making *Herschel* a five-band imaging camera spanning a decade in wavelength. Since the fields of view of the PACS and SPIRE cameras are offset by $\sim 20'$ in the plane of

the sky, slight oversizing of the individual observing tiles was needed to ensure that a $2^\circ \times 2^\circ$ area was covered in all five photometric bands.

As the bolometers that constitute the elemental pixels of the PACS and SPIRE arrays are differential detectors known to be affected by slow thermal drifts with typical $1/f$ frequency behaviour, each tile was observed in two independent passes with nearly orthogonal scanning directions. Individual astronomical observation requests (AORs) were concatenated in the *Herschel* observation planning tool (HSpot) so that the two scanning passes were executed immediately one after the other for each tile. This strategy was chosen so that a given position in the sky was observed by as many pixels as possible and in different scanning directions, producing the degree of redundancy needed to beat down the correlated and uncorrelated $1/f$ noise of single detectors, thereby allowing recovery of all the emission at the largest possible spatial scales. The approach was also designed to perfectly couple to the data processing and map-making pipeline specifically developed for the Hi-GAL project (see Sect. 3).

The satellite scan speed in pMode was set to its maximum value of 60 '' per second, with a detector sampling rate of 40 Hz for PACS and 10 Hz for SPIRE. The spatial sampling is therefore 1.5'' and 6.0'' for PACS and SPIRE, respectively, enough to Nyquist sample all the nominal diffraction-limit beams ($\approx [6.0, 12.0, 18.0, 24.0, 35.0]''$ at $[70, 160, 250, 350, 500] \mu\text{m}$, respectively). However, because of the limited transmission bandwidth, the PACS data were co-added on-board *Herschel*, with a compression of eight and four consecutive frames at 70 and 160 μm , producing an effective spatial sampling of 12'' and 6'' at 70 and 160 μm respectively. Therefore, in pMode, the PACS beams are not Nyquist sampled and the resulting point-spread functions (PSFs) are elongated along the scan direction with a measured size of $5.8'' \times 12.1''$ and $11.4'' \times 13.4''$ at 70 μm and 160 μm , respectively (Lutz 2012²).

Table C.1 summarizes a few details of the observations. Column 1 is an assigned field name for each tile, Cols. 2–5 report the approximate coordinates of the tile centre, Cols. 6 and 7 indicate the date of the observation for each tile, both in standard format and in OD number (observation day, starting from date of launch), Cols. 8–10 report the start time (UT) of the tile in the nominal and orthogonal scan direction (see below), together with the associated observation identification (OBSID) number uniquely attached to each scan observation.

SPIRE was used in bright-source mode in the three tiles of the survey closest to the Galactic centre (roughly centred at longitudes $+2^\circ, 0^\circ$ and -2°). This was done to avoid the widespread saturation and non-linearities in the detector response that are otherwise likely to occur on the extraordinarily strong background emission in that region. In this observing mode, the limited 12-bit dynamical range of the analog-to-digital converters in the detector chains is centred around higher-than-nominal current values. In this way, saturation is avoided at the cost of greatly decreased sensitivity. In bright-source mode SPIRE is much less capable of detecting intermediate and low-flux compact sources (see Fig. 20, last three panels).

3. Production of the photometric maps

The data reduction was carried out using the ROMAGAL data-processing software described in detail in Traficante et al. (2011). In short, the pipeline uses standard *Herschel* interactive

¹ Accessible from the VIALACTEA project portal at <http://vialactea.iaps.inaf.it>

² http://herschel.esac.esa.int/twiki/pub/Public/PacsCalibrationWeb/bolospf_20.pdf

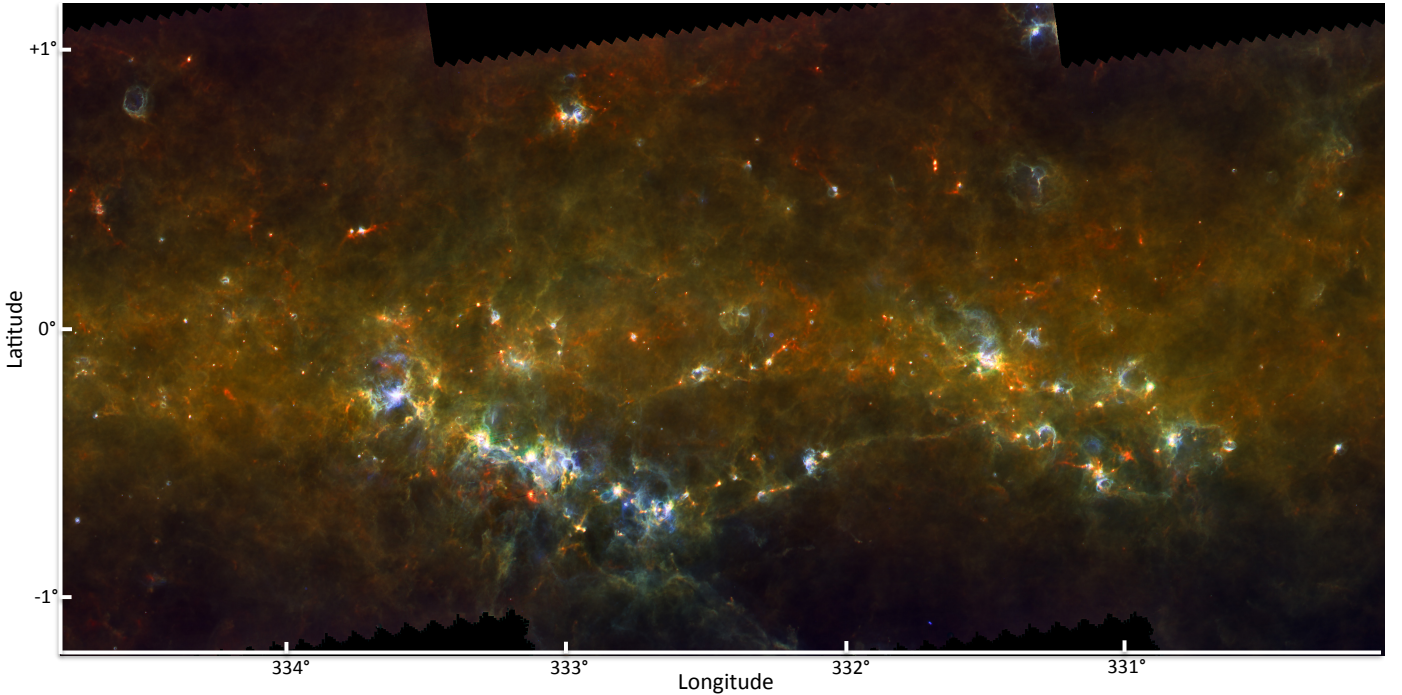


Fig. 1. Three-colour image (blue 70 μm , green 160 μm , red 350 μm) of a three-tile mosaic field around $330^\circ \lesssim \ell \lesssim 335^\circ$.

processing environment (HIPE) (Ott 2010) processing up to level 0.5, where the signal from individual detectors is photometrically calibrated and each detector has its sky position assigned. Subsequent steps in the data reduction were carried out using a dedicated pipeline written by the Hi-GAL consortium. Fast and slow detector glitches arising from particle hits onto the detectors are identified and the affected portions of the data are flagged in each detector's time ordered data (TOD). Slow detector drifts arising from $1/f$ noise are estimated and subtracted; for PACS, the drifts are estimated at subarray level as each 16×16 array matrix shares the same readout electronics. The core of the map-making implements a generalised least-squares (GLS) algorithm that is ideally designed to use redundancy to minimise residual uncorrelated $1/f$ detector noise by filtering in Fourier space (Natoli et al. 2001). To deliver optimal results, the code (i.e. each GLS-based code) requires that the detector noise properties are regularly sampled in time over the entire duration of the observations. For this reason, we implemented a pre-processing stage where the sections of the TOD flagged as bad data (e.g. due to a glitch removal or signal saturation) are replaced with artificial samples in which the data are set to 0, but where the noise is added using a constrained noise realisation using the noise frequency properties estimated from valid data immediately before and after the flagged section.

The pixel sizes of the ROMAGAL maps account for the larger-than-nominal PACS PSFs and are set to [3.2, 4.5, 6.0, 8.0, 11.5]'' at [70, 160, 250, 350, 500] μm respectively. This choice represents a good compromise between the need to sample the PSF as also determined for point-like objects in Hi-GAL maps with at least three pixels, while avoiding (for PACS 70 μm and 160 μm) excessively small pixels in which the hit statistics of the detector sampling are too low, resulting in increased pixel-to-pixel noise. For the PACS bands this arises because the *Herschel* scanning strategy in pMode implements an on-board frame co-adding (see Sect. 2), resulting in an effective decrease in sampling rate. The pixel size of the images is therefore such that the beam FWHM is sampled with three pixels for the three SPIRE

bands and with 2.66 pixels in the PACS bands. Saturated pixels in the maps are a consequence of signal saturation for all TODs covering the specific pixel, which is due to the necessary limitations in the dynamical range of DAC converters at the detection stage. A list of locations where saturation is reached is reported in Appendix B.

It is clearly not possible to report even in electronic form the complete list of images for all wavelengths and all the tiles of Table C.1 in this paper. We choose here to show only one figure (Fig. 1) as a three-colour image of a three-tile mosaic in the longitude range $330^\circ \lesssim \ell \lesssim 335^\circ$ to set the framework for the subsequent sections (see Sects. 4 and 5.1), describing the properties of the compact-source catalogues. The maps deliver a stunning view of the GP at all Hi-GAL wavelengths with a detail that is unattainable from any ground-based millimetre-wave facility now and in the foreseeable future. Extended emission with at least two orders of magnitude dynamical range in intensity is retrieved at all spatial scales from the most compact objects to the extent of the entire tile. We show in the next sections that compact sources within these multiple complex, extended structures have a very low peak-to-background contrast ratio (generally below 1). This makes the detection and flux computation of compact sources an extremely complex task, where it is in particular difficult to identify a figure of merit that can be used to unambiguously distinguish reliable from unreliable sources.

The pipeline is augmented with a module specifically developed by the Hi-GAL team to compensate for the high-frequency artefacts that the GLS map-making technique used in ROMAGAL (as in many other approaches, like MadMap or Scanamorphos) is known to introduce to the maps, namely crosses and stripes corresponding to the brightest sources. The left panel in Fig. 2 shows a typical example of these features that are introduced by the noise filter deconvolution carried out by the GLS map-maker in Fourier space when the flux is strongly varying with position, as is the case for point-like sources. We find that the minimum within a negative cross feature is proportional to the peak brightness of the source and amounts to $\sim 2.5\%$ of this

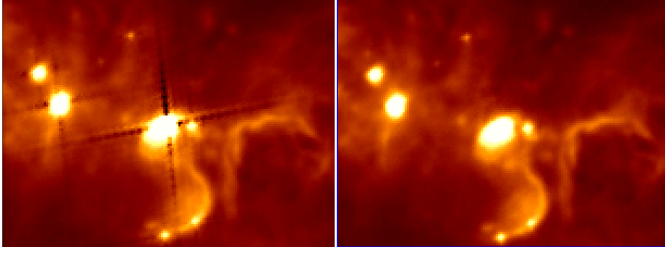


Fig. 2. *Left panel:* particulars of a point source as reconstructed by the ROMAGAL map-making for PACS at 70 μm ; the typical cross feature introduced by the GLS map-maker when performing the noise filter deconvolution in Fourier space over strongly varying signal (as is the case for point-like sources) is clearly seen (image in log scale). The minimum within the negative cross scales as $\sim 2.5\%$ of the peak source flux. *Right panel:* same as left panel with the same scale and colour stretch, but after applying the correction devised by [Piazzo et al. \(2012\)](#). The angular extent of the region imaged is $\sim 6' \times 4'$.

value. It is therefore not a strong effect in principle, but it can be quite annoying for relatively faint nearby objects and for the determination of the surrounding diffuse emission; it is also aesthetically undesirable.

To correct for these effects, which are particularly visible in the PACS 70- μm , and to a lesser extent, in the 160- μm images, a weighted post-processing of the GLS maps (WGLS, [Piazzo et al. 2012](#)) was applied to finally obtain images from which these artefacts are removed (right panel in Fig. 2).

3.1. Noise properties of the Hi-GAL maps

To characterise the noise properties of the Hi-GAL DR1 maps, we considered all the tiles in each band, locating and analysing those map regions where the lowest signal is found. This was done by computing the pixel brightness distribution and selecting pixels where the brightness was below the lowest 10 percentiles. We subsequently considered always for each tile and each band separately only those pixels that formed connected areas with at least 100 pixels each. In these we computed the median of the brightness and the mean of its rms. These quantities are reported in Fig. 3 as full and dashed lines as a function of Galactic longitude. The figure reports for each band the distribution of the lowest brightness levels and the corresponding rms found in each tile. The coloured ticks on the right margin of the figure represent the 1σ brightness sensitivities in MJy/sr predicted by the PACS and SPIRE time estimator for the Hi-GAL observing strategy, with two independent orthogonal scans taken in parallel mode at a scanning speed of $60'' \text{ s}^{-1}$.

Brightness levels are always well above the instrument sensitivities, showing that even in the faintest regions mapped by Hi-GAL, we are limited by cirrus brightness and cirrus noise emission by big grains ([Desert et al. 1990](#)) for $\lambda \geq 160 \mu\text{m}$, except perhaps at the outskirts of the Hi-GAL DR1 longitude range, where the minimum signal rms is close or equal to the predicted detector noise. An exception is the 70- μm emission, where the brightness of the diffuse cirrus that dominates at longer wavelengths drops significantly ([Bernard et al. 2010](#)). The 70- μm brightness levels reach (or cross) the respective rms values much earlier, moving away from the Galactic centre, than in the other bands. The fact that the most intense emission is reached at 160 μm and then decreases toward 500 μm is in excellent agreement with expectations for diffuse, optically thin cirrus dust at

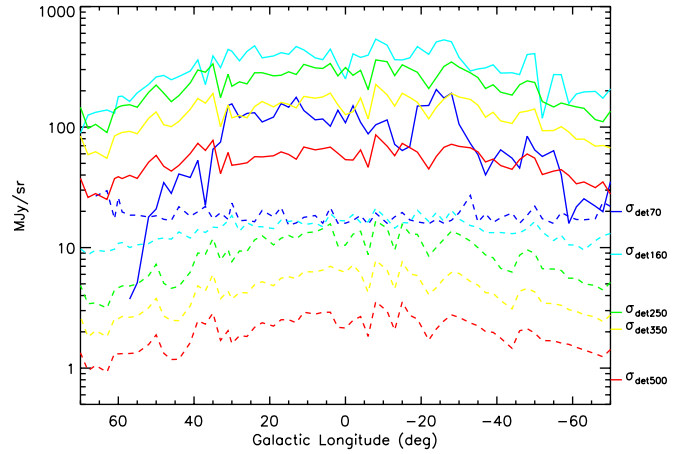


Fig. 3. Distribution as a function of Galactic longitude of the median brightness (full lines) and its rms (dashed lines) in regions within each Hi-GAL tile where the brightness levels are below the 10 percentiles of the brightness distribution for that tile. Hi-GAL bands are colour-coded as follows: blue for PACS 70 μm , cyan for PACS 160 μm , green for SPIRE 250 μm , yellow for SPIRE 350 μm , and red for SPIRE 500 μm . Ticks on the right margin of the figure mark the values of the theoretical sensitivities predicted by the official PACS/SPIRE time estimator (available in HSpot) for observations in pMode with $60'' \text{ s}^{-1}$ scanning speed.

temperatures $16 \text{ K} \lesssim T \lesssim 20 \text{ K}$, as determined by [Paradis et al. \(2010\)](#) from detailed modelling of Hi-GAL data in selected regions of the GP.

It should be noted that the Hi-GAL ROMAGAL pipeline used for DR1 is successfully delivering the PACS and SPIRE predicted sensitivities with the very bright and complex ISM emission on the GP, while preserving in the data processing chain the signal at all spatial scales with no spatial scale filtering.

3.2. Astrometric corrections

Although the map-making algorithm was run for each tile using the same projection centre for all bands, the PACS and SPIRE maps are slightly misaligned, possibly due to a residual uncalibrated effect in the basic astrometric calibration that is carried out in the HIPE environment. Excellent map alignment is essential to generate products such as column-density maps (e.g. [Elia et al. 2013](#)) or to positionally match source counterparts at different wavelengths.

As the images obtained with the same instrument (PACS or SPIRE) are internally aligned, we initially aligned the PACS 70 μm images to match the astrometry of the *Spitzer*/MIPSGAL images at 24 μm . This has the advantage that the two instrument/wavelength combinations deliver the same spatial resolution. The astrometric accuracy of the MIPSGAL images with respect to higher resolution IRAC and 2MASS is better than $\sim 1''$ on average ([Carey et al. 2009](#)).

For each tile, we visually selected a number of sources across the maps (typically more than six) that appear relatively isolated and compact both at 24 and 70 μm . The implicit assumption is that the two counterparts are the same physical source. This is reasonable as long as we avoid selecting sources in relatively crowded star-forming regions where sources in different evolutionary stages (and hence intrinsically different SED shapes) are generally found. We extracted the selected sources in both images and determined an average $[\delta l, \delta b]$ shift to minimize the

offsets between the positions of the selected sources in the 24- μm and 70- μm maps. This mean shift correction was then applied to the astrometric keywords in the FITS headers of the PACS maps.

The SPIRE maps were aligned by bootstrapping from the aligned PACS images. For each tile we selected a number of sources that appeared compact and isolated both in PACS 160 μm and SPIRE 250 μm . In a similar way to the alignment of the 70- μm PACS images, we extracted the selected sources in both maps and compared the source positions in the two bands to determine an average shift that minimizes the positional differences. This average shift was then applied to correct the astrometric keywords in the FITS headers of all SPIRE maps.

The corrections estimated for each tile are shown in Fig. 4 for PACS (cross signs) and SPIRE (triangles) images, taking the *Spitzer*/MIPSGAL images as a reference. Corrections can be as large as 6'' in absolute terms, meaning they are particularly significant for the PACS 70- μm band where they can reach about two-thirds of the image reconstructed FWHM beam width. The outlier point at the top right corner of the plot corresponds to the tile centred at $\ell = 299^\circ$, which was taken during the *Herschel* performance verification phase. The *Herschel* astrometric accuracy evolved throughout the mission because sources of errors in the star trackers and in general in the pointing reconstruction have been isolated and recovered. One of the main problems up to OD 320 were the speed bumps that caused large variations in the scanning speed of the telescope. These bumps occurred when a tracking star passed over bad pixels of the optical telescope's CCD. This effect was corrected for by lowering the operational temperature of the tracking telescopes. In general, the astrometric accuracy up to OD 320 was better than 2 arcsec, but outliers at more than 8 arcsec were observed (for a detailed report on the *Herschel* astrometric accuracy see Sánchez-Portal et al. 2014).

The error bars in Fig. 4 represent the rms of the source coordinates used to estimate the offset corrections with respect to their mean value. The distribution of these values is reported in the lower panels of Fig. 4; they are centred around the median values $[\Delta\text{GLON}, \Delta\text{GLAT}] = [0''.9, 0''.8]$ for the PACS images (lower left panel of Fig. 4), and $[1''.7, 1''.6]$ for the SPIRE images (lower right panel), and may be considered an estimate of the typical residual uncertainty of the source coordinates. These amount to $\sim 10\%$ of the PSF FWHM as estimated from compact sources in the images. It is interesting to note that there are a few outliers in the distributions, particularly apparent for the PACS shifts, but even for their maximum values they are below half of the PACS beam at 70 μm . As mentioned at the beginning of the section, an additional average 1'' uncertainty should be added in quadrature to account for the MIPSGAL pointing accuracy.

3.3. Map photometric offset calibration

Although the PACS and SPIRE images are calibrated internally in Jy/pixel and Jy/beam, respectively, their zero point level is not. To bring the images to a common calibrated zero level, an offset was therefore applied to the maps. The photometric offsets of the Hi-GAL maps were determined through a comparison between the Hi-GAL data and the *Planck* and IRIS (improved reprocessing of the IRAS survey) all-sky maps, following the procedure described in Bernard et al. (2010). We smoothed the *Herschel* maps to the common resolution of the IRIS and *Planck* high-frequency maps of 5' and projected them into the HEALPix pixelisation scheme (Górski et al. 2005) following the drizzling procedure described in Paradis et al. (2012), which preserves the photometric accuracy of the input maps. These smoothed

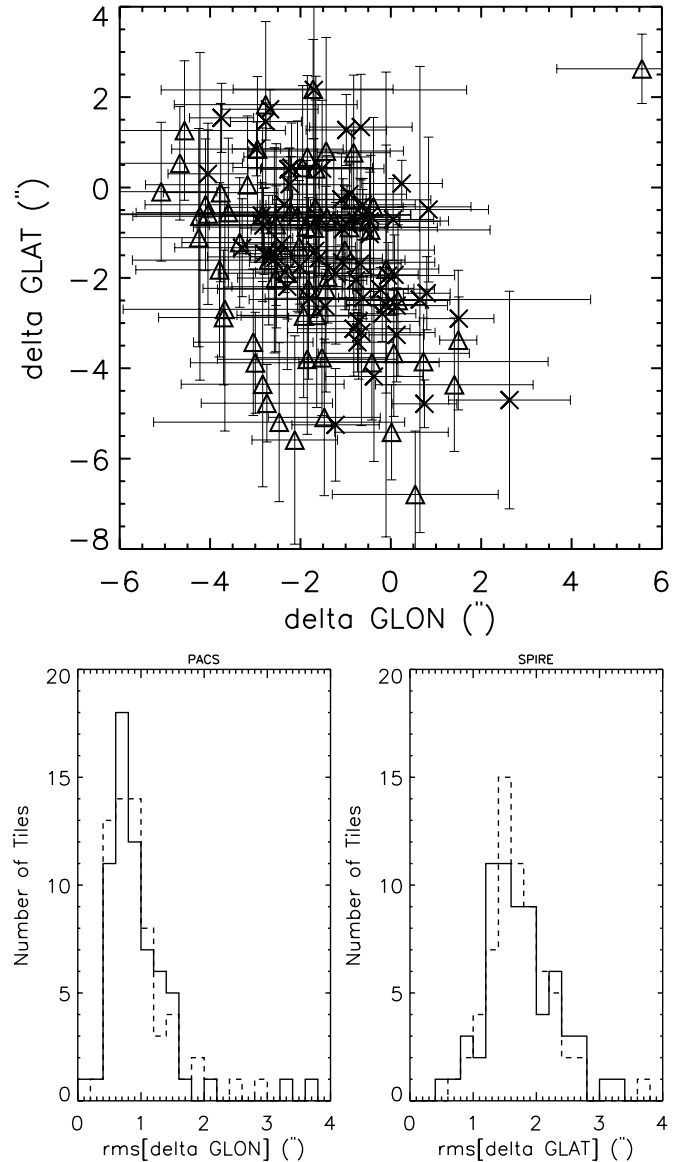


Fig. 4. *Top panel:* astrometry shifts in Galactic longitude (x axis) and latitude (y axis), estimated for each tile in arcseconds. Crosses are for PACS tiles while triangles are for SPIRE tiles. The error bars represent the rms of the source coordinates used to estimate the offset corrections with respect to their respective mean value. *Bottom panels:* histograms of the rms of the longitude (full lines) and latitude (dashed lines) shifts estimated for PACS (*left panel*) and SPIRE (*right panel*).

Hi-GAL maps are compared with the IRIS and *Planck* all-sky maps (hereafter called “model”).

To make this model, we used the IRIS maps projected into HEALPix taken from the CADE web site³ and the *Planck* maps shown in Planck Collaboration IX (2011). Since the *Herschel*, *Planck*, and IRAS photometric channels are different, the comparison requires frequency interpolation with differential colour correction and the use of a model. We predicted the shape of the emission spectrum in each pixel using the DustEM⁴ code (Compiègne et al. 2011), computed for an intensity of the radiation field best matching the dust temperature, derived from the combination of the IRIS 100- μm and the *Planck* 857-GHz

³ <http://cade.irap.omp.eu>

⁴ See <http://dustemwrap.irap.omp.eu/> and <http://www.ias.u-psud.fr/DUSTEM/>

and 353-GHz maps. The dust temperature assumed is that of [Planck Collaboration IX \(2011\)](#) with the standard dust distribution of [Compiègne et al. \(2011\)](#). For a given PACS or SPIRE band, the model was normalized to the data at the IRAS or *Planck* band at the nearest frequency to the considered *Herschel* band, and a predicted 5' resolution model image was constructed. These nearest frequencies are the IRAS 60- μm and *Planck* 857-GHz bands for the PACS 70- μm and 160- μm bands, respectively, and the *Planck* 857-GHz, 857-GHz, and 545-GHz bands for the SPIRE 250- μm , 350- μm , and 500- μm bands, respectively. In this process, the differential colour correction between IRAS or *Planck* and the *Herschel* band under consideration was also taken into account using the spectral shape predicted by the model on a pixel-by-pixel basis.

This resulting model image was compared with the smoothed Hi-GAL data through a linear correlation analysis, the intercept of which provides the offset level to be added to the *Herschel* data to best match the IRIS and *Planck* data. This analysis also provides gain corrections (i.e. a slope of unity between the data and the model), but these are well below the cumulative relative uncertainties in the datasets used and in the dust modelling assumptions, and within 10%, on average, in all bands. The standard *Herschel* photometric calibration was therefore assumed, and no additional gain corrections were applied. We also note that the *Planck* data used do not have the same absolute calibration as the publicly available version. A forthcoming processing of the Hi-GAL data will use the latest *Planck* calibration and will allow for a global gain correction.

4. Generation of photometric catalogues from Hi-GAL maps

In comparison to the ground-based submillimetre-continuum surveys, the *Herschel* instruments do not suffer from the need to correct for varying atmospheric emission and absorption, allowing recovery of the rich and highly structured large-scale emission from Galactic cirrus and extended clouds. Such variable and complex backgrounds, however, severely hinder the use of traditional methods to detect compact sources based on the thresholding of the intensity image. Such methods are widely used by large-scale millimetre and radio surveys from ground-based facilities, such as the Bolocam GPS ([Rosolowsky et al. 2010](#)), CORNISH ([Purcell et al. 2013](#)), or ATLASGAL ([Contreras et al. 2013](#)), where diffuse emission is filtered out either by atmospheric variation correction or the instrumental transfer function. The possibility of processing *Herschel* images using high-pass filtering was discarded for various reasons. First of all, it would be difficult to choose a threshold in spatial scale. Dust cores and clumps are compact but, depending on their distance and physical scale, may not be point-like (i.e. unresolved). A spatial filtering scale threshold too close to the PSF will remove power from compact but resolved sources, while a threshold high enough to ensure that no power is removed from scales corresponding to two to three times the PSF will prove ineffective to improve source detection in crowded fields. A second reason is that any high-pass spatial filtering will introduce negative lobes with intensities proportional to the brightness of the extended emission, severely hindering the detection of faint sources that fall within those features.

In a previous work, [Molinari et al. \(2011b\)](#) introduced a new method to detect sources and extract their fluxes tailored to the case of the complex and structured background present in IR/sub-mm observations. With respect to other popular

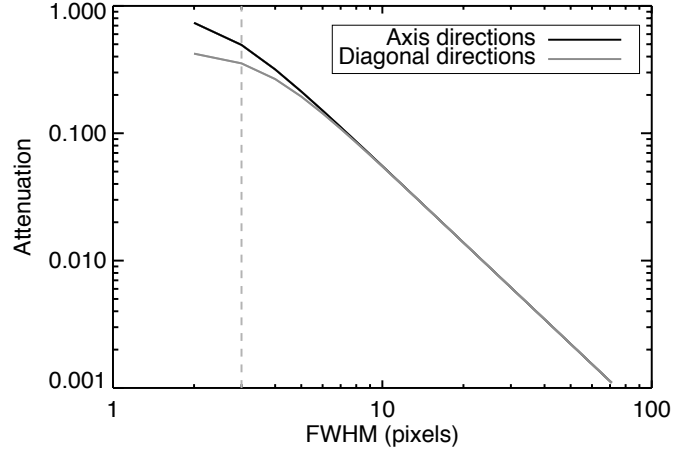


Fig. 5. Relative attenuation of the peak intensity induced by the derivative filtering as a function of the scale of the structure. The diagonal directions have been divided by $\sqrt{2}$ to take the longer distance along the diagonals with respect to the normal axis into account. For scales longer than ~ 6 pixels, the damping increases as a power-law function with an exponent -2 . The dark grey dashed line refers to the typical size in pixels of the PSF in Hi-GAL maps.

algorithms, the CuTex⁵ photometry code, standing for CURvature Thresholding EXtractor, adopts a different design philosophy, looking for the pixels in the map with the highest curvature by computing the second derivative of the map. All the clumps of pixels above a defined threshold are analysed, and those larger than a certain area are kept as candidate detections. The pixels of the large clumps are checked to determine enhancement of curvature in the case of multiple sources. For each detection, an estimate for the size of the source is determined by fitting an ellipse to the positions of the minima of the second derivative in each of the eight principal directions. The output fluxes and sizes are determined by simultaneously fitting elliptical Gaussian functions plus a second-order 2D surface for the background. All the sources whose detected centres are closer than twice the instrumental PSF are fitted together to separate their fluxes.

The Gaussian fitting was carried out for each source by considering a fitting window centred on each source and with a width of three times the instrumental PSF to ensure that we included sufficient space surrounding the source for a reliable estimate of the background. This has the drawback that the pixels used to constrain the background are numerically predominant with respect to the pixels characterising the source; to counterbalance this effect, the pixels located within a distance equal to the initial guess-estimated source size from the source position are given a higher weight in the fit.

4.1. Characterisation of the photometric algorithm

CuTex, as a derivative-based detection algorithm, acts as a high-pass spatial filter; however, contrary to simple median or boxcar filtering, derivative filtering has inherent multiscale capabilities by selectively filtering out the larger of the spatial scales in a continuous way with higher efficiency. This behaviour is shown in Fig. 5, where we report for Gaussians with increasing widths the ratio between the second derivative image and the original one at the peak position as a function of the spatial scale expressed in pixels. The results shown are obtained on a

⁵ See <http://herschel.asdc.asi.it/index.php?page=cutex.html>

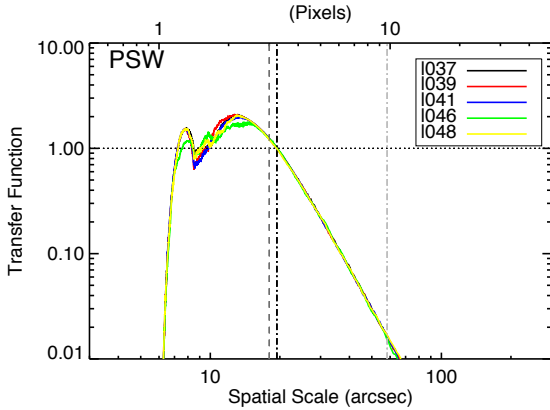


Fig. 6. Ratio between the power spectrum of the derivative images (averaged over the four directions) computed by CuTex and the power spectra of the intensity image for SPIRE 250 μm as a function of spatial scale expressed in arcseconds and in pixels (upper x axis). Each colour corresponds to a different map; black to the 1037, red to the 1039, blue to the 1041, green to the 1046, and yellow to the 1048 field. All the functions overlap for scales larger than the PSF, indicated as a dark grey dashed line, and decrease following a power law with an exponent ~ -3.9 . The black dot-dashed line indicates the scale at which the transfer function is equal to unity. Scales smaller than this result in an overall amplification in the second derivative maps. The light grey dot-dashed line traces the scale above which the extended sources become confused with the background in the derivative image. This value corresponds approximately to ~ 3 times the PSF. Similar plots are found for other wavelengths, and the functions completely overlap when the spatial scales are expressed in pixels.

simulated image where the FWHM of the PSF is sampled by three pixels, and therefore is a general result applicable to any map that shares this characteristic, like the *Herschel* maps we present here. Figure 5 shows that the peak intensity of a point-like source, with a FWHM of ~ 3 pixels (i.e. 1 PSF), is damped in the second derivative image to $\sim 40\%$ of its original value, while an extended source with FWHM of ~ 7.5 pixels (i.e. $2.5 \times$ PSF) and the same peak intensity is damped to $\sim 10\%$ of the original value. In other words, a point source in the intensity map that is ten times fainter (contrast 0.1), for instance, than the surrounding background, with a typical scale of order 15 pixels, that is, $5 \times$ PSF, will appear in the derivative map as ~ 1.7 times brighter than the background (contrast 1.7). Given the trend in Fig. 5, where attenuation decreases following a power-law behaviour with an exponent -2 , it is then possible to detect sources with less favourable contrast the larger the background typical scale. Clearly, the method has the inherent drawback of being most effective for more compact objects (see below).

To confirm the performances of CuTex's derivative operator for real maps, we computed the power spectrum of the second derivative image for each map, averaging the spectra obtained for each derivative direction. We then divided each derivative power spectrum by the power spectrum of the parent intensity image. These ratios are proportional to the module square of the transfer function of the derivative operator used by CuTex. Figure 6 shows these ratios for five different maps (indicated with different colours in the figure) for 250- μm observations. Similar plots are found for the other wavelengths, where the only difference is a shift in angular spatial scale that is due to the different pixel scales. The scale in the upper x axis is in pixels and insensitive to the specific pixel angular scale.

Several conclusions can be drawn from the analysis of these functions. First, the transfer function is the same, regardless of the mapped region, for scales larger than the PSF. Second, the damping introduced by the derivative operator found in Fig. 5 is also confirmed for real maps. From an investigation of a sample of very extended sources in the Hi-GAL maps, we estimated that CuTex is not able to recover most of the sources with sizes larger than three times the PSF (see also Fig. 18), being completely insensitive to any source larger than ~ 5 times the PSF. The third conclusion resulting from Fig. 6 is that the derivative filtering introduces an amplification for scales smaller than the PSF. This means that any pixel-to-pixel noise present in the intensity map is increased in the second derivative maps. Slight differences between the different tested fields are only visible at scales below the PSF (the dashed line in the figure) but are not relevant for the detection of real sources. To quantify this increase, we tested the effect of the derivative operator on pure Gaussian noise maps and found that the noise in the second derivative follows the same distribution, with a standard deviation 1.13 times the initial one. This behaviour is not unexpected because of the linearity properties of the derivative filtering.

4.2. Choice of the extraction threshold

In similar way to source extraction performed on images of surface brightness distribution, it is useful to set an extraction threshold as a function of the local curvature rms instead of adopting a constant absolute value. In this way, the depth of the extraction is adapted to the complexity of the morphological properties and to the intensity of the background that constitutes the dominant flux contribution in the far -infrared toward the GP.

Although the adoption of a detection threshold in the second derivative image is certainly less intuitive than adopting a threshold on the flux brightness map, we have shown above that the noise statistical properties do not change from flux maps to flux curvature maps (except for a small increase in the width of the noise distribution), so that the notion of a threshold that adapts to the local noise properties can also be applied to detection on the curvature images.

The choice of an optimal source extraction threshold always results from a compromise between the need to extract the faintest real sources and the need to minimize the number of false detections. Pushing the detection threshold to increasingly lower values to extract ever fainter sources is of course of minimal use if the majority of these faint extracted sources have a high probability of being false positives, therefore considerably limiting the catalogue completeness and reliability. Unfortunately, there is no exact way to control the number of false positives extracted from real images because there is no control list for real sources present, so that a number of a posteriori checks are needed to determine this optimal threshold value.

The procedure we adopted to estimate the optimal extraction threshold is to make extensive synthetic source experiments to characterise the flux completeness levels obtained for different CuTex extraction thresholds σ_c in all five Hi-GAL photometric bands, where σ_c is in units of the rms of the local values of the second derivatives of the image brightness averaged over four directions (see Molinari et al. 2011b).

As it is clearly impractical to make these studies over the entire set of Hi-GAL tiles, we chose three tiles at Galactic longitudes of 19, 30, and 59 degrees that are representative of the widely variable fore-to-background conditions that can be found

over the entire survey. For each of these tiles and for each observed band, hundreds of synthetic sources were injected at different flux levels. We then ran CUTEX for a set of extraction thresholds σ_c from 3 to 0.5, estimating for each threshold the flux for which 90% of the synthetic sources were successfully recovered. We verified that, for each of the three tiles, the 90% completeness fluxes decrease with decreasing extraction threshold. For the three SPIRE bands, we see that this decrease flattens, starting at $\sigma_c \sim 2$, meaning that we do not gain in depth of extraction at lower thresholds. We emphasise that our artificial source experiments provide the same optimal value for the extraction threshold independently of the tile used, in spite of the very different properties of the diffuse and structured background exhibited by the Hi-GAL images in the longitude range covered in DR1. This is a convenient feature of the detection method, which is clearly able to deliver similar performances with very similar parameters in widely different fields. We then adopted $\sigma_c = 2$ as the extraction threshold for the SPIRE bands.

For the PACS 70- μm and 160- μm bands, the decrease of the 90% completeness fluxes continues below $\sigma_c = 2$. This apparent gain in the number of reliable sources detected at increasingly lower thresholds is probably due to increasing numbers of false-positive detections. We characterise the effect of false positives by evaluating the number of extracted sources in the different bands as a function of the extraction threshold. Figure 7 top reports the number of sources detected in the three tiles (indicated by the different colours) at 70, 160 and 250 μm (solid, dashed, and dotted lines) as a function of the extraction threshold. The figure shows that in all cases the N - σ_c relations tend to become steeper below $\sigma_c \sim 2$; we emphasise this in Fig. 7 in one case by fitting two power laws to two portions of the N - σ_c for the 70 μm case of $\ell = 59^\circ$ (the two thin dotted lines). A similar behaviour is exhibited for all the other cases, and we interpret this increase of rate in detected sources for $\sigma_c \leq 2$ as an indication of increased contamination of false detections. It is, strictly speaking, impossible to verify this claim on real images because we do not have a truth table for the sources that are effectively present. We then used a subset of the extensive simulations performed in Molinari et al. (2011b), where we presented and characterised the CUTEX package; the bottom panel of Fig. 7 reports the number of true detected sources (full line) and the number of false positives (dashed line) as a function of the extraction threshold for a simulation of 1000 synthetic sources (that were reported in the top-left panel of Fig. 7 in Molinari et al. 2011b). This shows that for decreasing extraction thresholds, the number of false-positive detections increases faster than the number of real sources. It is irrelevant here to compare the absolute values of the slopes between the real and simulated cases in Fig. 7 or the thresholds where the false positives may become dominant because the two cases refer to very different situations (see Molinari et al. (2011b) for more information on the simulations carried out). It is important here that the faster increase of false positives with respect to real sources as a function of decreasing threshold may qualitatively explain the change of slopes in the detection rates with thresholds that we see in the real fields in the top panel of Fig. 7.

To be conservative for this first catalogue release, we chose to adopt an extraction threshold of $\sigma_c = 2$ also for the 70 μm and 160- μm PACS bands. The detection threshold might be pushed to lower values especially in the PACS bands and toward low absolute Galactic longitudes; this requires more extensive studies of the completeness level analysis and characterisations of the real impact of false-positives contamination, however, and is deferred to the release of subsequent photometric catalogues.

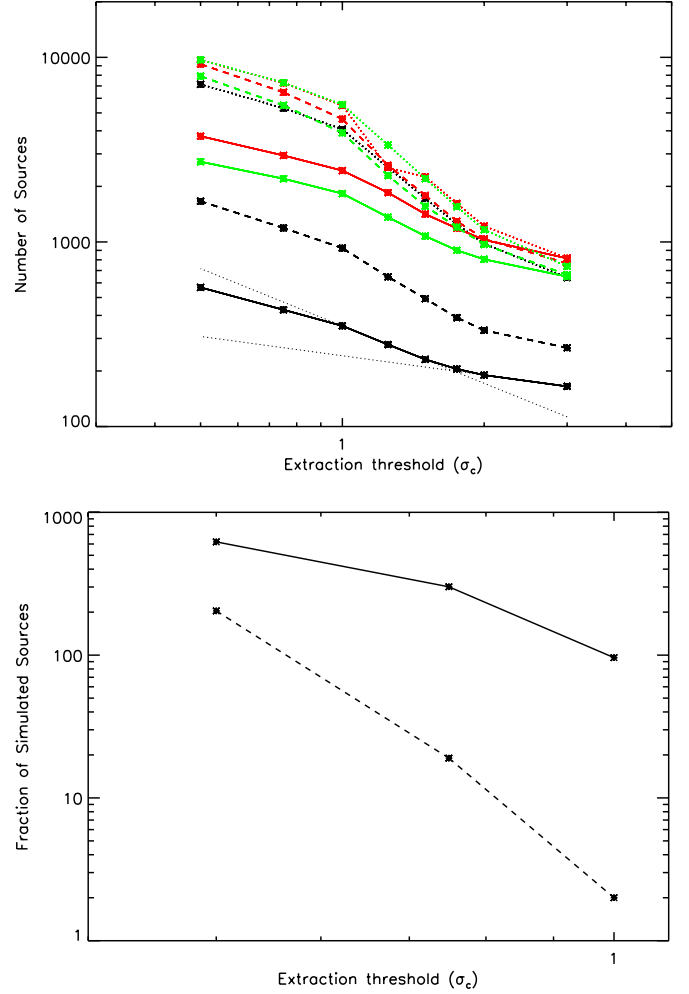


Fig. 7. *Top panel:* number of sources extracted with CUTEX as a function of extraction threshold for the 70 μm (thick solid lines), 160 μm (thick dashed lines), and 250 μm bands (dotted thick lines) for three Hi-GAL tiles with very different background conditions: $\ell = 19^\circ$ (green lines), $\ell = 30^\circ$ (red lines) and $\ell = 59^\circ$ (black lines). The thin dotted lines are power-law fits to the initial and mid portions of the N - σ_c relationship at 70 μm for the $\ell = 59^\circ$ tile and are shown to emphasise the change in slope that is visible for all functions for $\sigma_c \lesssim 2$. *Bottom panel:* detection statistics for the simulated source experiments reported in Fig. 7 of Molinari et al. (2011b) for a flux of 0.1 Jy; the total number of simulated sources is 1000. The full line reports the number of true sources recovered, while the dashed line reports the number of false positives as a function of extraction threshold. It is noticeable that the number of false positives increases faster for decreasing thresholds than the number of true sources detected, qualitatively explaining the change of slope in the real field detections (*top panel*).

4.3. Generation of the source catalogues

Sources were extracted independently for each Hi-GAL tile and for each band using CUTEX with an extraction threshold $\sigma_c = 2$. As each map tile results from the combination of two observations of the same area scanned in nearly orthogonal directions and since the area scanned in the two different directions is never exactly the same, the marginal areas of the combined maps will generally be covered in only one direction, resulting in very poor quality compared to the majority of the map area. For this reason, we excluded such areas from the source extraction. The selection of the optimal map regions was performed manually for each tile and separately for the PACS and SPIRE images. These regions

Table 1. Source numbers in the Hi-GAL photometric catalogues.

Band	N_{sources}
PACS-70 μm	123, 210
PACS-160 μm	308, 509
SPIRE-250 μm	280, 685
SPIRE-350 μm	160, 972
SPIRE-500 μm	85, 460

will always be at the margins of the tiles, but this does not result in gaps in longitude coverage because the contiguous border region of any tile will be optimally covered by the adjacent tile.

The full source extraction was carried out on an IBM BladeH cluster with seven blades, each equipped with Intel Xeon Dual QuadCores, for a total of 56 processors. Each independent tile and band extraction job was dynamically queued to each processor, allowing us to complete the extraction from $63\ 2^\circ \times 2^\circ$ tiles in five bands in one day. The different photometry lists for each band were then merged together to create complete single-band source catalogues. As there is always a small overlap between adjacent Hi-GAL tiles, some sources may be detected in two tiles. In this case, where source positions matched within one half of the instrumental beam, the detection with the higher signal-to-noise (S/N) ratio was accepted into the source catalogue. The number of compact sources extracted over the longitude range considered in this release are reported in Table 1.

The CuTEX algorithm detects sources by thresholding on the values of the curvature of the image brightness spatial distribution, and as such is optimised to detect compact objects that may be more extended than the instrumental beam. The analysis reported in Sect. 4.1 shows that the second-order derivative processing ensures differential enhancement of smaller spatial scales with respect to larger scales also above the instrumental PSF. In Sect. 5.3 we verify that the majority of extracted sources have sizes that span the range between 1 and 3 times the instrumental PSF, with most of the objects below 2–2.5 times the beam (see Fig. 18) and axis ratio below 2 (see Fig. 19). In the rest of the paper we refer to the compact source catalogues to signify that the catalogues include relatively round objects with sizes generally below 2–2.5 times the beam.

The catalogues contain basic information about the detection and the flux estimation for all sources, including source position, peak, and integrated fluxes, estimated source size and uncertainty computed as the brightness residuals after subtracting the fitted source+background model. The calibration accuracy of the PACS photometer is of about 5% in all bands (Balog et al. 2014) because of the uncertainties in the theoretical models of the SED of the stars used as calibrators. For SPIRE the main calibrator is Neptune and, as for PACS, the main uncertainty comes from the theoretical model of the planet emission and is estimated at 4% in all the bands (Bendo et al. 2013).

Hi-GAL photometric catalogues are ASCII files in IPAC table format and contain information on source position, peak, and integrated fluxes, source sizes, locally estimated noise and background levels, and a number of flags to signal specific conditions found during the extraction. The full list of the 60 table columns, with explanation of the column contents, can be found in Appendix A. The number of columns prevents us from showing a preview of the catalogue tables in printed form. The single-band photometric catalogues are delivered to ESA for release

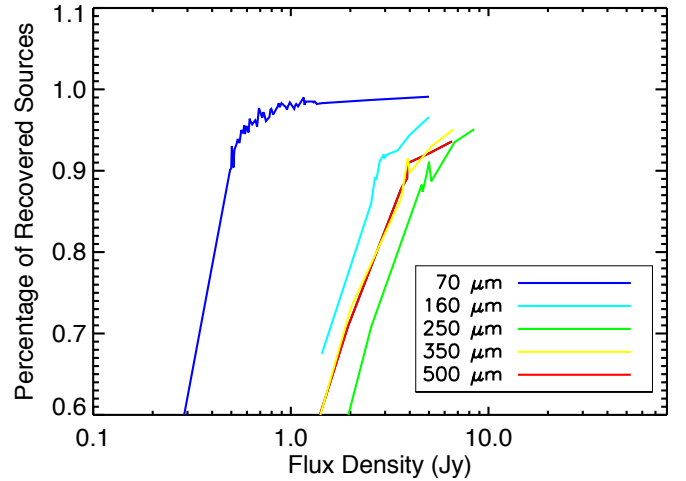


Fig. 8. Completeness fractions as a function of flux density for the map centred at $(\ell, b) = (19, 0)$, a field with a very intense and complex background at the boundary of the central molecular zone, in the different *Herschel* bands for sources with statistically the same sizes as those in the extracted catalogue.

through the *Herschel* Science Archive and are available via a dedicated image cutout and catalogue retrieval service¹.

4.4. Catalogue flux completeness

To quantify the degree of completeness of the extracted source lists, we carried out an extensive set of artificial source experiments by injecting simulated sources into real Hi-GAL maps. Given the very time-consuming nature of these experiments, we chose to carry them out for each band, but only for a subset of the entire range of longitudes that is the subject of the present release. We visually selected one from every two to three tiles, depending on the variation of the emission seen in the maps as a function of Galactic longitude. We used a similar methodology as in Sect. 4.2 to determine the optimal extraction threshold, but this time we used only one detection threshold and an adaptive grid of trial fluxes for the synthetic sources.

For each band of this subsample, we injected 1000 sources modelled as elliptical Gaussians of constant integrated flux, with sizes and axis ratios equal to the majority of the compact sources determined from the initially extracted list (see Figs. 18 and 19). In this way, we were able to test the ability to recover a statistically comparable population of sources from the same map. The sources were randomly spread on the map, with the only constraint being to avoid overlap with the positions of the real sources.

The simulated data were processed with CuTEX, adopting the same setup of parameters as used for the initial list, and the outputs were compared with the truth table of the injected sources. To estimate the errors, we iterated the experiment ten times and determined the variation in the fraction of recovered sources. The same process was iterated for different values of integrated flux until we recovered 90% of the sources (with a tolerance of 1%). An example of the recovery fraction as a function of the integrated flux density of the injected sources is given in Fig. 8.

In Fig. 9 we show the estimated completeness limit as a function of Galactic longitude. The limits for the PACS 70 μm and 160 μm bands are quite regular along the whole range of

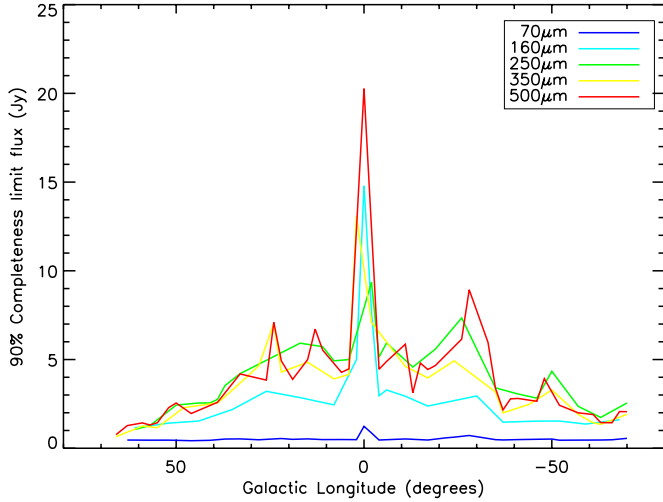


Fig. 9. Ninety percent completeness limits in flux density for a population of sources with the same distribution of sizes as the one extracted by CUTEX as a function of Galactic longitude. The significant increase in the completeness limit in the inner Galaxy and especially close to the Galactic centre is due to the brighter background emission in such regions.

longitude. However, while the completeness in the 70 μm band is almost constant, at 160 μm it is higher for $|\ell| \leq 40^\circ$. This behaviour is more significant in the SPIRE wavebands and increases while moving toward the Galactic centre. It is explained by the overall brighter emission at lower longitudes, making the detection of fainter objects a harder task, even with the strong damping induced by CUTEX.

The completeness limits reported in Fig. 9 should be seen as conservative because they are determined by spreading the synthetic sources randomly over each entire tile. However, the diffuse background is highly non-uniform in each tile, but it is dominated by the strong GP emission with a maximum in the central horizontal section of each map, and then decreasing toward the north and south Galactic directions. A typical example is offered in Fig. 10, where the upper panel shows the 250 μm image of the tile centred at $\ell = 41^\circ$. Superimposed are the extracted 250 μm compact sources with integrated fluxes above (yellow crosses) and below (magenta crosses) the flux completeness limit appropriate for the Galactic longitude at that band (3 Jy, from Fig. 9). This is also shown in the lower panel of Fig. 10, where the latitude distribution of the two groups of sources is also reported with full and dashed lines for sources above and below the confusion limit.

The two groups of sources have a very different spatial distribution, with sources brighter than the completeness limit mostly concentrated at $-0.6 \leq b \leq 0.2$, while the fainter sources are uniformly distributed and mostly found toward the map areas where the diffuse emission is relatively less intense. The dashed line in the lower panel histogram is flat because fainter sources are better detected in lower surface-brightness regions (above and below the plane) than in the central band of the plane.

In subsequent releases of the Hi-GAL photometric catalogues we will provide more precise estimates of the catalogue completeness limits specific to different background conditions.

4.5. Deblending

CUTEX is designed to fit a Gaussian function to each position that shows an enhancement of the second derivative with

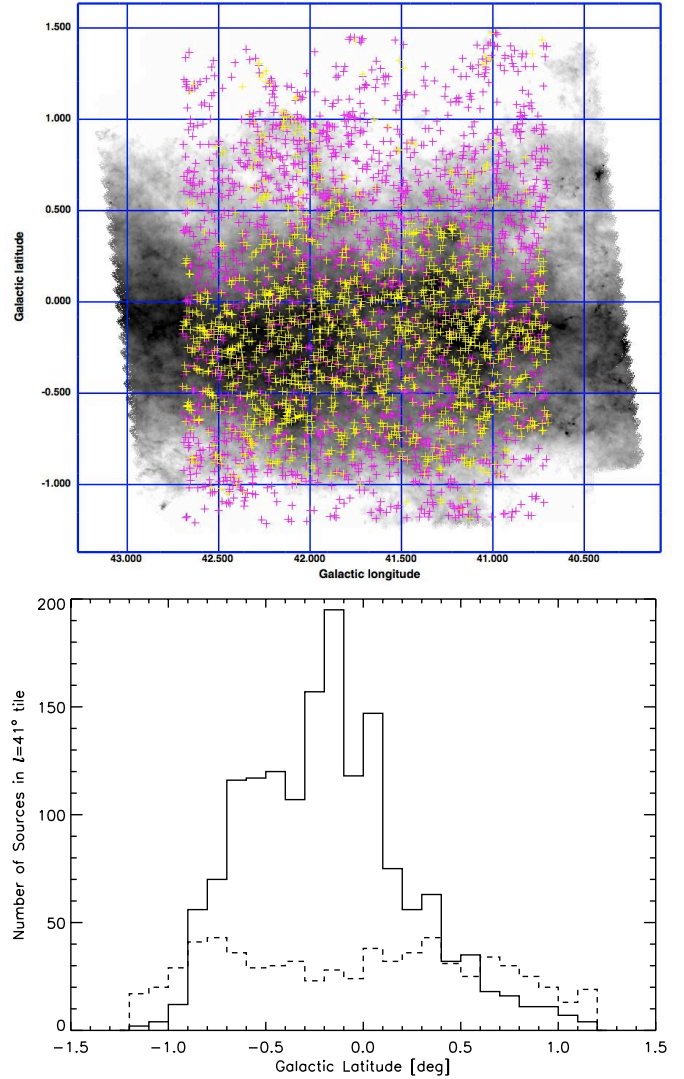


Fig. 10. Upper panel: 250 μm image of the Hi-GAL tile at $\ell = 41^\circ$. Superimposed are the sources detected with CUTEX. The yellow crosses indicate the sources with fluxes above the completeness limit, while the magenta crosses indicate the sources with fluxes below the completeness limit. Lower panel: histograms of latitude distributions for 250 μm sources, above (full line) and below (dashed line) the completeness limit.

respect to its nearby environment. While the flux estimate relies on the performance of the fitting engine as well as on the fidelity of the Gaussian model fit to the real source profiles, it is clearly important to quantify the ability of the photometric algorithm to separate individual sources when they are very close to each other. To quantify the deblending performance of the algorithm, we generated simulations with 2000 sources randomly distributed in a region whose size represents the typical footprint of the Hi-GAL maps. For every set of positions we produced two different sets of simulated populations. In the first case, we injected sources with sizes of the order of the beam size. In the second case we simulated a population of extended sources modelled as elliptical Gaussians with the FWHM of one of the two axes drawn from a uniform distribution between 1 and 2.5 times the beam size. The other axis was determined by assuming an axis ratio randomly drawn from a uniform distribution between 0.5 and 1.5 times the beam size. The input sources were randomly oriented. We computed several simulations with

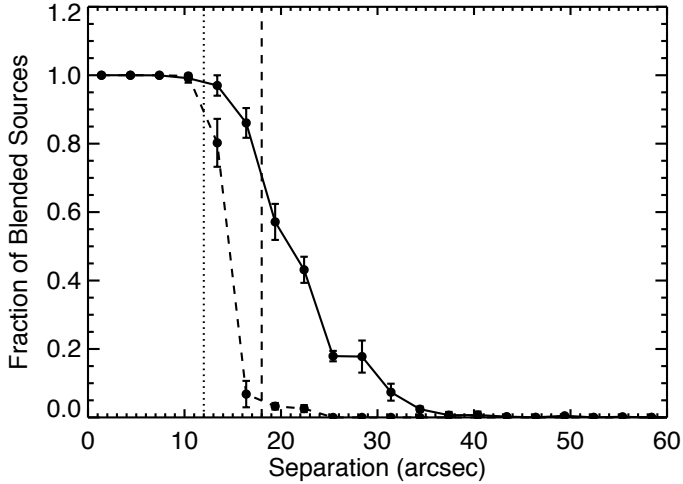


Fig. 11. Curves represent the fraction of blended sources that CuTEX is not able to deblend as a function of source separation for a set of synthetic sources described in the text; simulations in this case are made for the $250\ \mu\text{m}$ images. The full and dashed lines are the results for simulations with extended and point-like sources, respectively. Vertical lines represent the size of the beam (dashed), and 75% the size of the beam (dotted).

different positions and increasing source densities to estimate the deblending performance for cases of both lesser and greater clustering.

We processed the simulations with CuTEX and determined its ability to correctly identify individual sources as a function of the source pair separation. Because of the large number of sources and their relatively high densities, there are several thousand source pairs in each simulation that can be tested for the effectiveness of our deblending algorithm. We plot in Fig. 11 the fraction of source pairs that are not resolved into their separated components as a function of their relative separation for simulations of the $250\ \mu\text{m}$ data (where the maps have a pixel size of $6''$). Similar curves are found for the other wavelengths. The error bars represent the amplitude of such a fraction found in the whole set of simulations. The full line refers to the population of extended sources, while the dashed line indicates the results for the sample of point sources. The vertical dashed line traces the size of the beam, while the dotted line traces 0.75 times the beam.

Figure 11 shows that CuTEX is able to deblend sources quite effectively. Point-like sources are resolved perfectly up to distances that are ~ 0.8 times the beam, while extended sources are properly deblended and identified for distances larger than ~ 1.25 times the beam. For the extended source case, half of the source pairs that are separated by a single beam size are deblended. Clearly, the Gaussian fit for a blended source pair will result in a larger size estimate than the case where the two components are resolved by the detection algorithm.

4.6. Photometric corrections to integrated fluxes

The flux of the source candidates is derived from the parameters of the 2D-Gaussian fit found with CuTEX. While a 2D Gaussian is a good and acceptable approximation for the PSF of SPIRE (SPIRE Instrument Team & Consortium 2014), the same is not true for PACS because of the observing setup adopted for the Hi-GAL survey. The on-board coaddition (in groups of eight frames at $70\ \mu\text{m}$ and four frames at $160\ \mu\text{m}$) while scanning

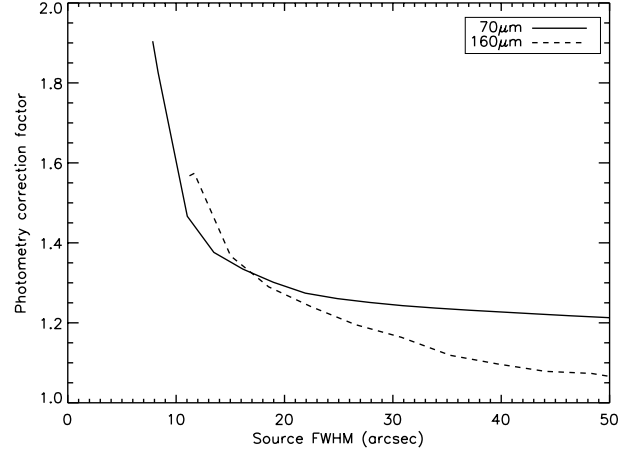


Fig. 12. Correction factors to be applied to CuTEX photometry as a function of the source FWHM. The values are only applicable for images obtained similarly to Hi-GAL.

the satellite, results in substantially elongated beams (see Sect. 2 above) that show significant departures from a circularly symmetric morphology. Part of this asymmetry is mitigated by the coaddition of scans in orthogonal directions, but significant departures from an ideal Gaussian symmetry persist. It is then necessary to estimate correction factors to be applied to the extracted CuTEX photometry to account for the (incorrect) assumption of Gaussian source brightness profiles assumed by CuTEX.

We adopted an empirical approach to estimate the corrections to the CuTEX photometry of PACS images. This was done by performing CuTEX photometry, using the same settings as used for the Hi-GAL catalogues, on an image of a primary *Herschel* photometric calibrator – α Bootis. α Bootis was observed during OD 269 in the same conditions as the Hi-GAL observations (i.e. with two mutually orthogonal scan maps in parallel mode with a scanning speed of $60''/\text{s}$). The α Bootis images present a nice and clean point-like object with no detectable diffuse emission background (ideal photometry conditions compared to Hi-GAL). To extend the photometric correction factors to the more general case of compact but resolved sources, we convolved the images of α Bootis with a 2D-circular Gaussian kernel of increasing size while normalizing integrated flux (i.e. flux conserving). The convolving kernels span the interval $[0.0, 5.0] \times \theta_0$ in steps of $0.5\theta_0$, where θ_0 is the FWHM derived from the unconvolved α Bootis profile. CuTEX integrated fluxes for the entire set of simulations were then compared with the expected values in the PACS bands as derived from theoretical models (Müller et al. 2014). After applying a colour correction estimated following Pezzuto et al. (2012), the fluxes of α Bootis used for the comparison are 15.434 and 2.891 Jy at 70 and $160\ \mu\text{m}$, respectively. Figure 12 reports the correction factors as estimated from the above analysis as a function of the FWHM of the compact source considered. The correction factors decrease rapidly from point-like to minimally resolved sources. With larger sources, the decrease in the correction factor is a weaker function of source size. Beam asymmetries, however, are clearly persistent and detectable even for relatively extended sources.

The integrated fluxes for each source in the 70 and $160\ \mu\text{m}$ catalogues were corrected using the curves in Fig. 12 and the sources' circularised size (see Sect. 5.3). Both the uncorrected and the corrected integrated fluxes are reported in the columns FINT and FINT_UNCORR of the source catalogues

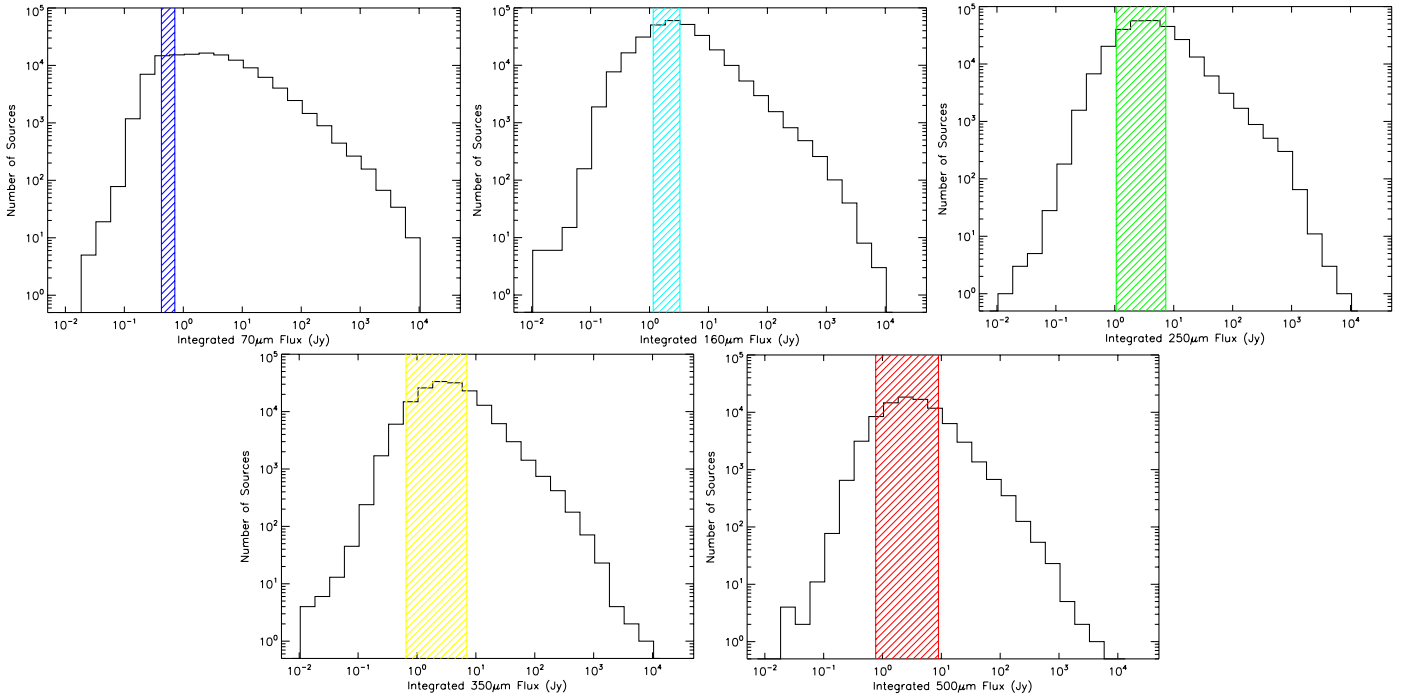


Fig. 13. Histograms of the integrated flux F_{Int} for all Hi-GAL compact sources in the five bands for the entire DR1 survey area. Flux completeness limits vary with Galactic longitude (see Fig. 9); the spanned longitude range (with the exception of the central $|l| \leq 2^\circ$) is reported by the colour-coded and shaded areas in Fig. 9.

(see Appendix A). We emphasise that these correction factors are only valid for images obtained from two scan maps taken in orthogonal directions in pMode with a $60''/\text{s}$ scanning speed, and for sources extracted using a 2D Gaussian source model (i.e. they are not valid if PSF-fitting or aperture photometry is performed). The same analysis was carried out for SPIRE, but the correction factors estimated were largely within 10% for the unconvolved α Bootis image, confirming the reliability of the Gaussian approximation for the SPIRE beams. Larger sources could not be simulated because of the high spatial density of background compact objects of extragalactic origin but, as suggested by Fig. 12, the effect should be even lower.

5. Properties of the compact source catalogues

5.1. Source fluxes and reliability

In Fig. 13 we report the distribution of the integrated fluxes of all extracted compact sources in the five photometric bands. The histograms report the sources detected within the entire DR1 survey area. The large spread in detected fluxes, while representative of the entire survey, does not necessarily reflect the flux distribution in any individual tile. For example, the sources in the faint tail of the distributions originate mainly from the tiles at higher longitudes and are not detected in tiles like the one at $[l, b] = (19^\circ, 0^\circ)$ for which we report the completeness limits in Fig. 8, or from regions that are removed from the central latitude band around $b = 0^\circ$. In addition, the objects at the far left side of each histogram (low flux) are those that are potentially most affected by false positives, as discussed in Sect. 4.2. We note, however, that even if we combine the sources in the four left-most bins of each histogram in Fig. 13, these sources combined only account for 0.8% of the total number of sources in the $70 \mu\text{m}$ band and for less than 0.1% for the other bands.

It is difficult to identify a parameter that can be uniquely taken as a measure of the reliability of a source detection. It is important to remember that the background conditions found at *Herschel* wavelengths in the Galactic plane are totally unprecedented. Therefore, criteria based on the S/N of the detected sources (that are reliable criteria in conditions of absent or low background), for example, are not straightforward to apply because compact sources have a variety of sizes (see Sect. 5.3) and are located on a Galactic ISM background that shows spatial variations at all scales. Figure 14 illustrates the relation between the background-subtracted peak flux densities of the sources and the intensity of the underlying background emission as estimated during the 2D Gaussian fitting in CUTEX. A direct relationship between the two quantities is apparent in all bands, and Fig. 14 furthermore shows that the peak flux of the sources is always a factor of a few fainter than the value of the background. An additional problem is that not only does the background dominate the source peak fluxes, but its fluctuations increase with the absolute level of the background. Therefore, since the uncertainties in the extracted source fluxes are computed starting from the residuals obtained after subtracting the fitted source+background (the latter modelled with a second-order surface) from the original maps, the magnitude of the residuals will be higher the higher the absolute level of the background. This is shown in Fig. 15, where the rms of the fitted residuals is reported for the various bands as a function of the absolute level of the fitted background.

The result is that even relatively very bright objects will have a limited S/N. We plot in Fig. 16 the relationship between the integrated fluxes and their uncertainties. These uncertainties are the estimated rms of the image residuals computed by subtracting the source as fitted and integrating the residual over the source's fitted area. We see that a large majority of the extracted sources have $S/N \geq 3$ (the blue line in the figure), but rarely does the S/N exceed ~ 10 . This is the effect of the complex background, which makes it difficult to estimate source sizes or even

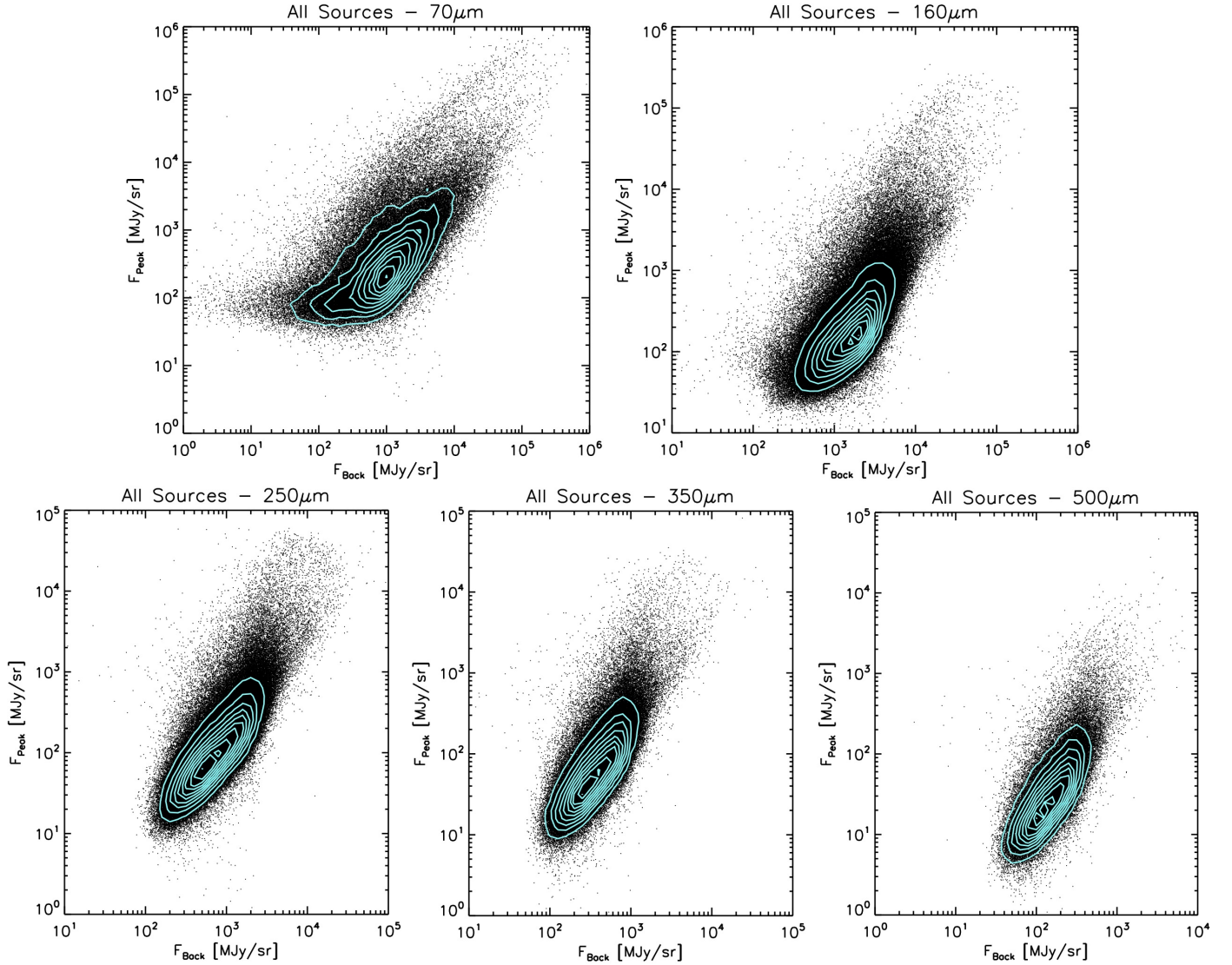


Fig. 14. Background-subtracted source peak flux density F_{Peak} as a function of the flux density of the underlying background F_{Back} , as estimated by the source fitting for all Hi-GAL bands as indicated. The ten cyan contours (equally spaced in source density) indicate the source density in the most crowded area. Note that the axis scale is not the same in all panels.

to effectively represent the underlying background during the source fitting process in analytical form. Therefore, it is possible that even relatively good contrast sources may have low S/Ns. For example, Fig. 17 left shows source 117 in the 250 μm band, which has a peak/background contrast of ~ 1 (which is relatively high compared to the average conditions represented in Fig. 14), but whose S/N is only ~ 2 . Upon visual inspection, however, the source detection appears entirely reliable. This reinforces the notion that the quoted uncertainties should not be taken as a direct indication of the reliability of a source detection, but solely of the reliability of the estimated integrated flux. In other words, it may be difficult to estimate a high-fidelity flux even for a bright source, given the intensity and complexity of the background found in the far-IR in the Galactic plane.

It might be tempting then to adopt the contrast value as a simple-to-use quality indicator for the reliability of a source. Unfortunately, there are also several cases where relatively low-contrast sources have high S/Ns. This is demonstrated in Fig. 17 right, where source 1251 has a contrast of ~ 0.15 , but a $S/N \sim 13.5$. We therefore find ourselves in the very difficult situation

for this release to be unable to define any combination of parameters that may offer a reliable quality flag for all detected sources. We therefore issue this first release of the Hi-GAL catalogues with a strong caveat; for the moment, there is no easy shortcut to identify the most reliable sources other than attempting combinations of various parameters (which likely may give good results for certain background conditions, but poor results in others) followed by visual inspection of the maps. A blind selection of sources with high S/N will certainly result in reliable samples, but will miss many reliable objects.

This may be mitigated by cross-matching sources in different bands. The green points in Fig. 16 represent the subset of all sources for which a counterpart can be positionally matched (see Elia et al., in prep.; Martinavarro-Armengol et al., in prep.) in at least two adjacent wavelength bands. The fact that virtually all the green points are above the $S/N = 3$ line is an indication that a positive match with counterparts in other bands is, at present, most likely the best criterion to ensure the reliability of both the detection and the flux estimate for a source. Several sources that appear with high S/N at 70 and 160 μm in Fig. 16 do not show

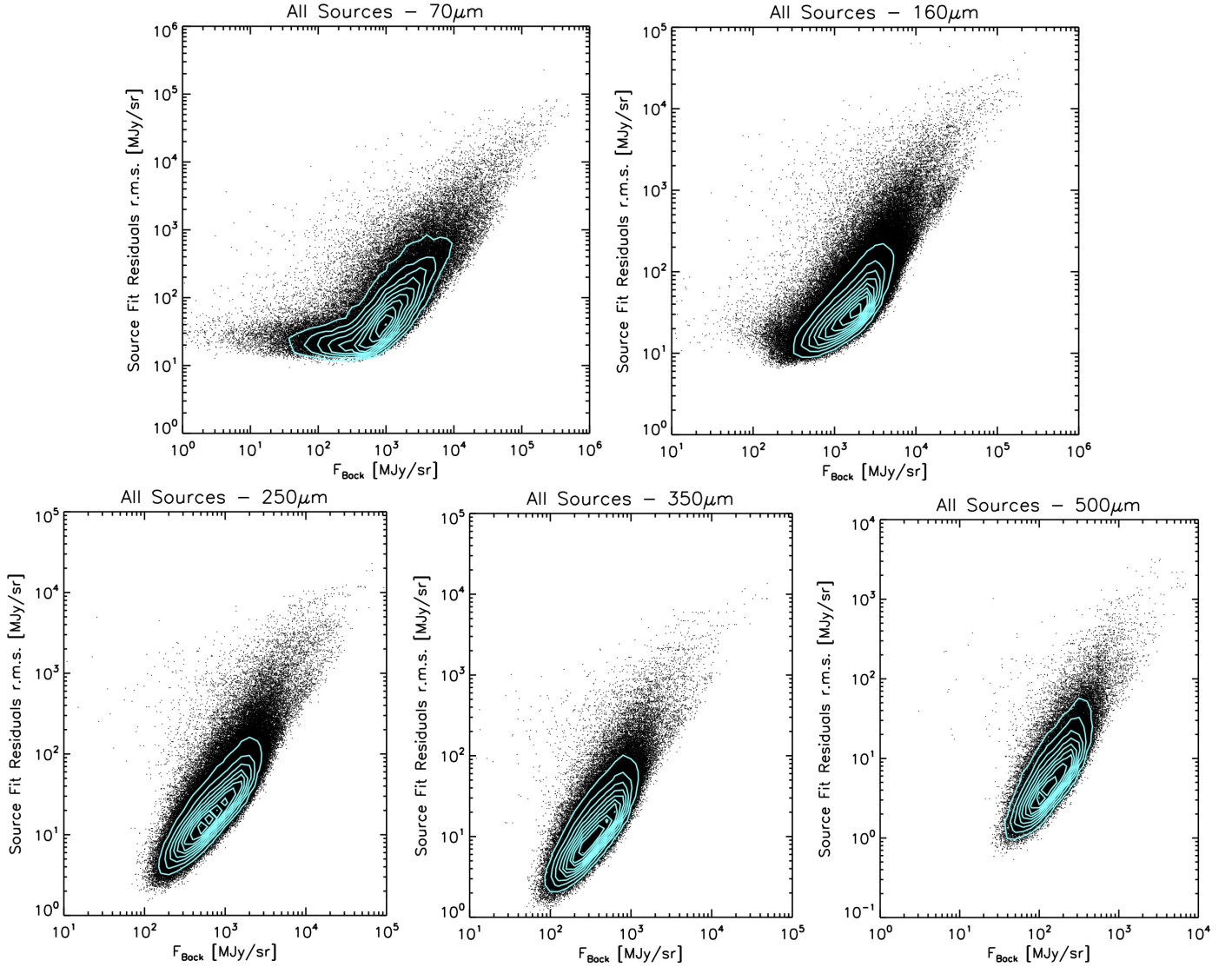


Fig. 15. Rms of the flux density residuals after subtracting the fitted source+background as a function of the flux density of the underlying background F_{Back} , as estimated by the source fitting for all Hi-GAL bands as indicated. The ten cyan contours (equally spaced in source density) indicate the source density in the most crowded area. Note that the axis scale is not the same in all panels.

counterparts in at least three Hi-GAL bands (i.e. the black dots above $S/N = 3$). For the greater part, these sources have relatively strong counterparts at shorter wavelengths and exhibit SEDs that decrease longward of $100 \mu\text{m}$ and are not detected at SPIRE wavelengths. More complete statistics in this respect will be presented by Elia et al. (in prep.) and Martinavarró-Armengol et al. (in prep.), who will discuss the Hi-GAL photometric catalogues in the context of ancillary photometric Galactic plane surveys such as ATLASGAL (Schuller et al. 2009), MIPS GAL (Carey et al. 2009), and others. We emphasise once more that some of the sources with $S/N \geq 3$ and with counterparts in three adjacent bands (the green points) have integrated fluxes below the completeness limit pertinent to the specific Galactic longitude if the source is located more than $0.3\text{--}0.4$ degrees latitude on average off the midplane.

As experience accumulates in the use of these catalogues, we plan to improve the quality assessment for the catalogue sources in subsequent data releases. Ultimately, since there may be no better instrument to judge the reliability of a source than an astronomer’s trained eye, a possible strategy could be to deploy

machine-learning capabilities. In these techniques, input from a trained user would teach the algorithm to search for specific patterns in the combination of catalogue parameters, thereby allowing it to automatically identify sources that should be discarded.

5.2. Contamination from extra-galactic sources

Although the Galactic plane is inarguably the most unfavourable environment in which to detect galaxies, there is no doubt that background galaxies could, in principle, contaminate the detection of Galactic sources in Galactic plane surveys (Marleau et al. 2008; Amores et al. 2012). To evaluate the degree of possible contamination from galaxies in our photometric catalogues, we took advantage of the shallow cosmological surveys carried out by *Herschel* using the same observing mode as we used for Hi-GAL. Rigby et al. (2011) reported the photometric catalogues for the science demonstration phase fields of the H-ATLAS survey with SPIRE (Eales et al. 2010), showing that at $250 \mu\text{m}$ the density of extragalactic sources with an integrated flux higher than 0.1 Jy is of the order of 10 deg^{-2} . The

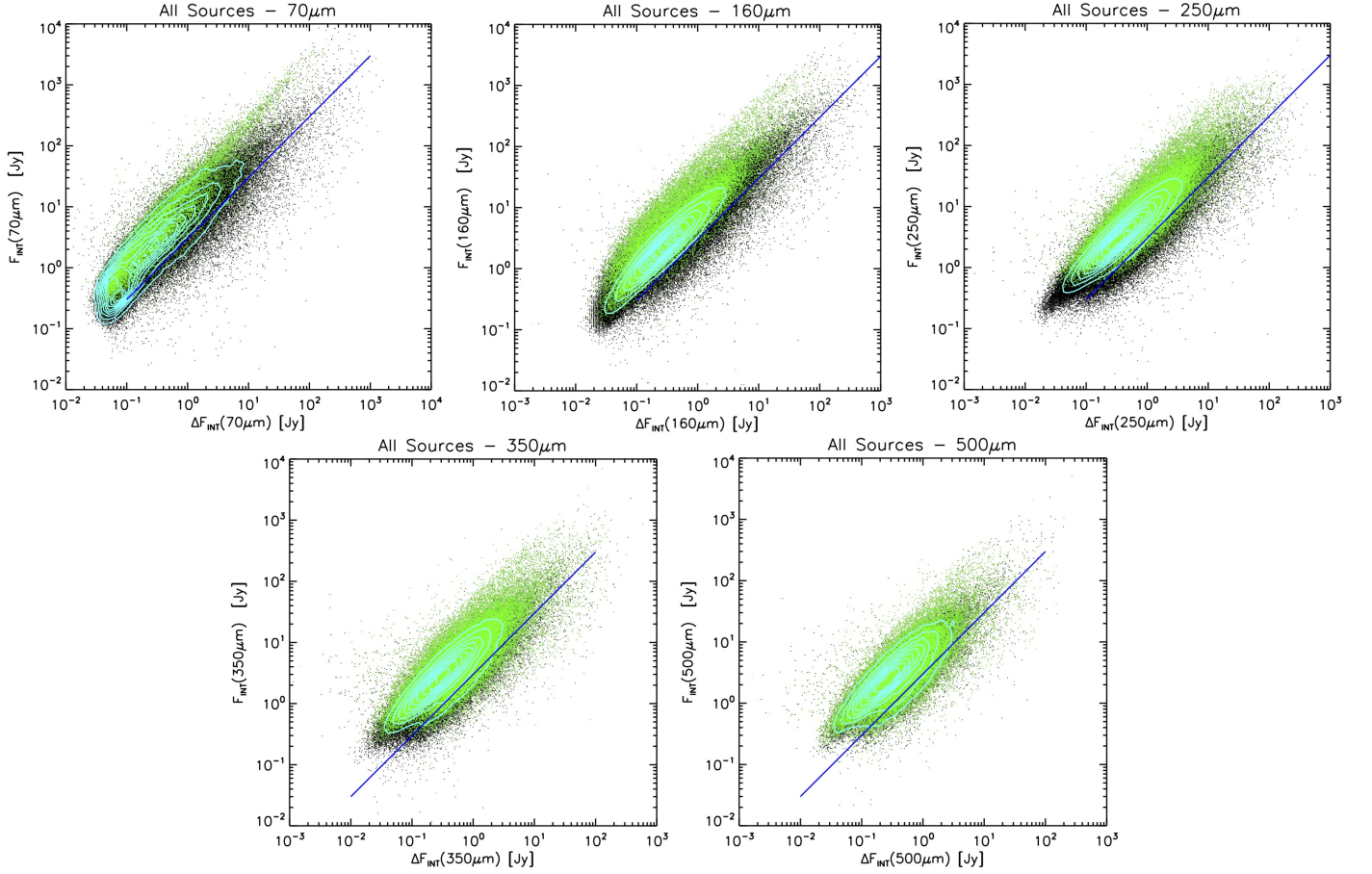


Fig. 16. Integrated flux F_{Int} as a function of its uncertainty ΔF_{Int} for all Hi-GAL bands as indicated. The black points are all the sources in each band catalogue; the ten cyan contours (equally spaced in source density) indicate the source density in the most crowded area. The green points are the subset of sources that possess a counterpart in at least two adjacent bands (so as to form an SED with at least three photometric points, see Elia et al., in prep.). The blue line represents $S/N_{\text{Int}} = 3$.

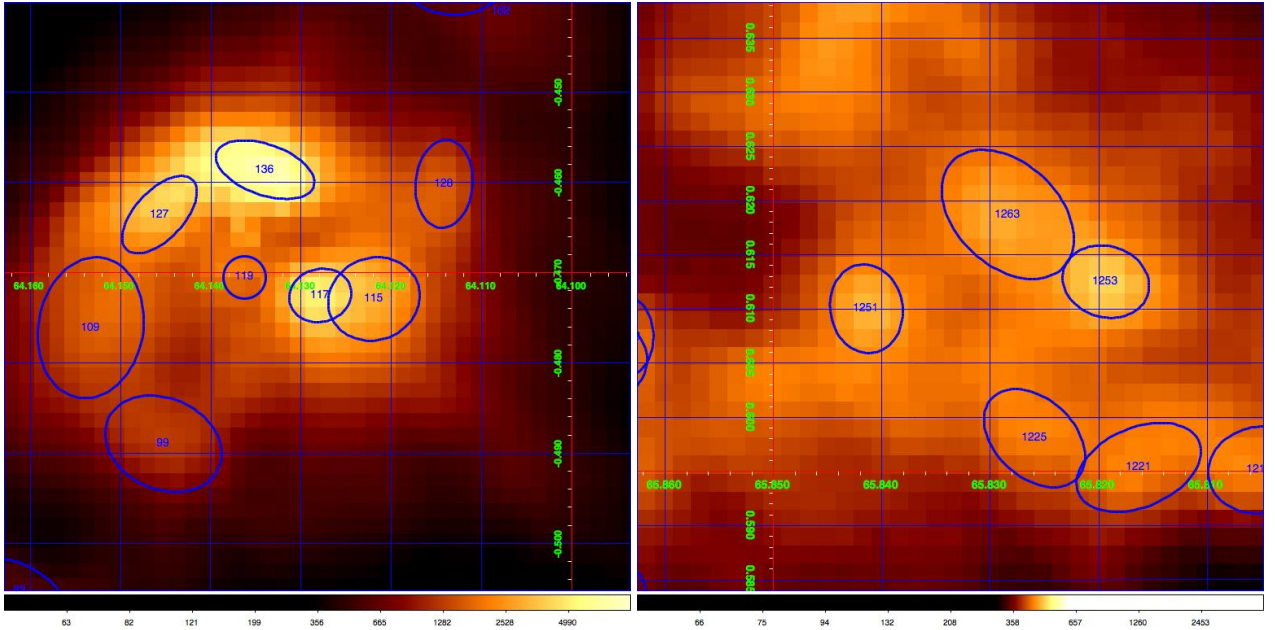


Fig. 17. Left panel: case of a source at $250\mu\text{m}$, labelled 117, in which the peak/background contrast is ~ 1 (hence relatively high, see Fig. 14), but the S/N is only 2.1. Right panel: case of a source at $250\mu\text{m}$, labelled 1251, with a very good S/N of 13.5, but with peak/contrast ratio ~ 0.15 .

distribution of the integrated fluxes in the $250\ \mu\text{m}$ Hi-GAL catalogues reported in Fig. 13 shows that basically all (99.98%) of the $\sim 280\,000$ sources detected at $250\ \mu\text{m}$ have fluxes above $0.1\ \text{Jy}$; as the present catalogue release encompasses a surveyed area of ~ 270 square degrees, the average density of the $250\ \mu\text{m}$ Hi-GAL sources is therefore $\sim 1000\ \text{deg}^{-2}$. The average contamination from extragalactic sources is, therefore, $\leq 1\%$ at $250\ \mu\text{m}$. Using the same method, the contamination fractions at the other SPIRE wavelengths are $\leq 0.7\%$ at $350\ \mu\text{m}$ and $\leq 0.3\%$ at $500\ \mu\text{m}$. Given the shape of extragalactic source counts (see Rigby et al. 2011), these estimated contaminations are concentrated toward the faint end of the Hi-GAL source catalogues. The extragalactic source density decreases by one order of magnitude from 0.1 to $0.4\ \text{Jy}$, while the number of Hi-GAL $250\ \mu\text{m}$ sources above $0.4\ \text{Jy}$ is still 99.3% of the total. Therefore, contamination effect from extragalactic background sources is negligible and limited to integrated fluxes below $0.4\ \text{Jy}$ at $250\ \mu\text{m}$. The situation is even more favourable at the other SPIRE wavelengths. This is marginally visible in the histograms of Fig. 13.

For the PACS bands, Lutz et al. (2011) provided photometric catalogs from the PEP program, which surveyed well-known cosmological fields. About 125 sources with fluxes above $0.1\ \text{Jy}$ at $160\ \mu\text{m}$ are detected in the $2.78\ \text{sq. deg.}$ PEP fields, corresponding to about $45\ \text{deg}^{-2}$. Using the same approach as for the SPIRE bands, this corresponds to a contamination fraction from extragalactic sources of about 4%. However, the PEP PACS maps were taken in prime mode with a scan speed of $20''/\text{s}$, achieving much higher sensitivities than in parallel mode observations, especially in the virtually background-free conditions typical of cosmological fields. Lutz et al. (2011) quoted 3σ noise levels of $8\ \text{mJy}$, which agrees very well with the expected noise levels predicted by the HSpot tool for the PEP observing mode at the centre of the maps where the coverage is higher. On the other hand, the HSpot tool provides a 1σ sensitivity of $\sim 46\ \text{mJy}$ at $160\ \mu\text{m}$ for observations in parallel mode, or a factor ~ 16 poorer than for observations in prime mode. If we artificially degrade the flux uncertainties reported by Lutz et al. (2011) by this factor, the number of sources that would have been detected at a 3σ level would decrease from 125 to 29, bringing the contamination level down to $\leq 1\%$. PEP $70\ \mu\text{m}$ source catalogues have been made available for the GOODS-S field only (Lutz et al. 2013), and only one source has been detected with a flux greater than $0.1\ \text{Jy}$, which is not a large enough sample with which to assess possible contamination. Given this single detection, however, we deem the contamination to be negligible in this band.

We conclude that contamination from distant background galaxies is extremely low and concentrated toward the faint end of the flux distribution of the Hi-GAL sources. This effect is, perhaps, visible in Fig. 13 as a tentative flattening of the flux distributions at $F_{\text{int}} \leq 0.1\ \text{Jy}$ for the 160 , 250 , and $350\ \mu\text{m}$ bands. Local Universe galaxies have higher fluxes, but are also far from compact and have a very low spatial density (see Ciesla et al. 2012 and Boselli et al. 2010). Therefore, it is unlikely that they have been included in the present catalogue.

5.3. Source sizes

Figure 18 reports the distribution of the circularised source sizes in the different bands, calculated by taking the square root of the product of the major and minor axis as estimated by CUTEX. Source sizes span a range of values, from that of the PSF to about twice the PSF for most of the sources. The broad distributions in Fig. 18 show that the sources are generally mildly resolved, with the exception of the $70\ \mu\text{m}$ band, where a peak at the PSF value

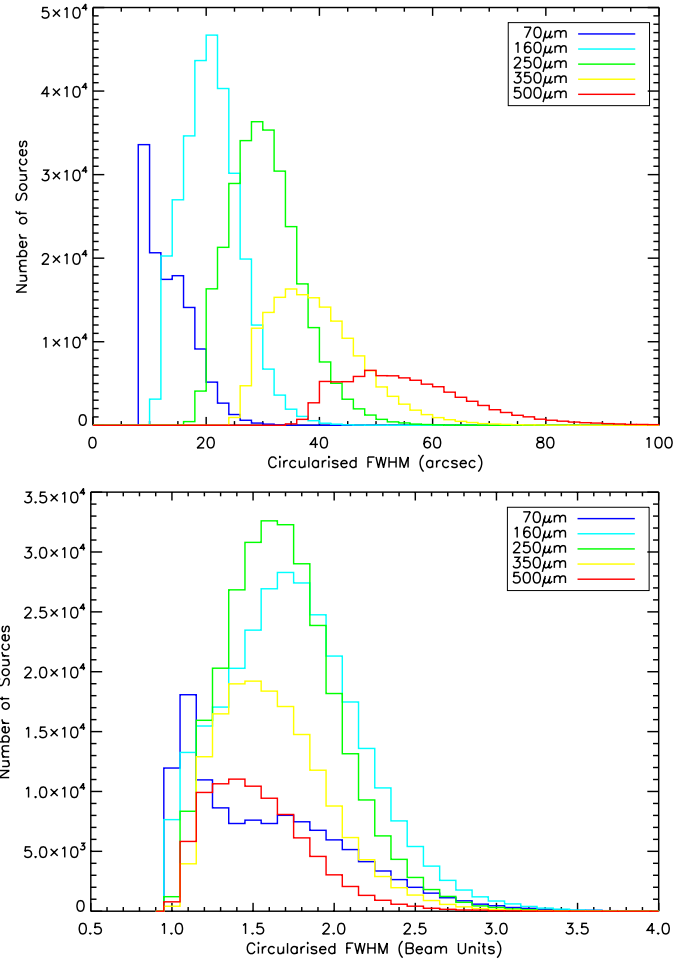


Fig. 18. *Top panel:* distribution of the circularised FWHM of the catalogue sources in the five bands. Sizes are computed as the geometric mean of the FWHMs estimated by 2D Gaussian fitting in two orthogonal directions. *Bottom panel:* same as above, but in units of the beam size.

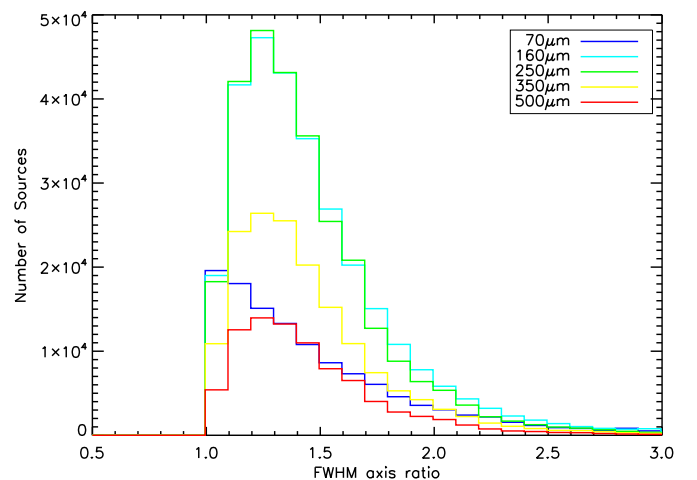


Fig. 19. Distribution of the axis ratio, computed as the ratio of $FWHM_{\text{Maj}}/FWHM_{\text{min}}$ of the catalogued sources in the five bands.

is clearly visible. We stress that Fig. 18 reports the circularised sizes; sources may be unresolved in one direction and resolved in the other, therefore resulting in being moderately resolved on average. This is confirmed by Fig. 19, showing that extracted

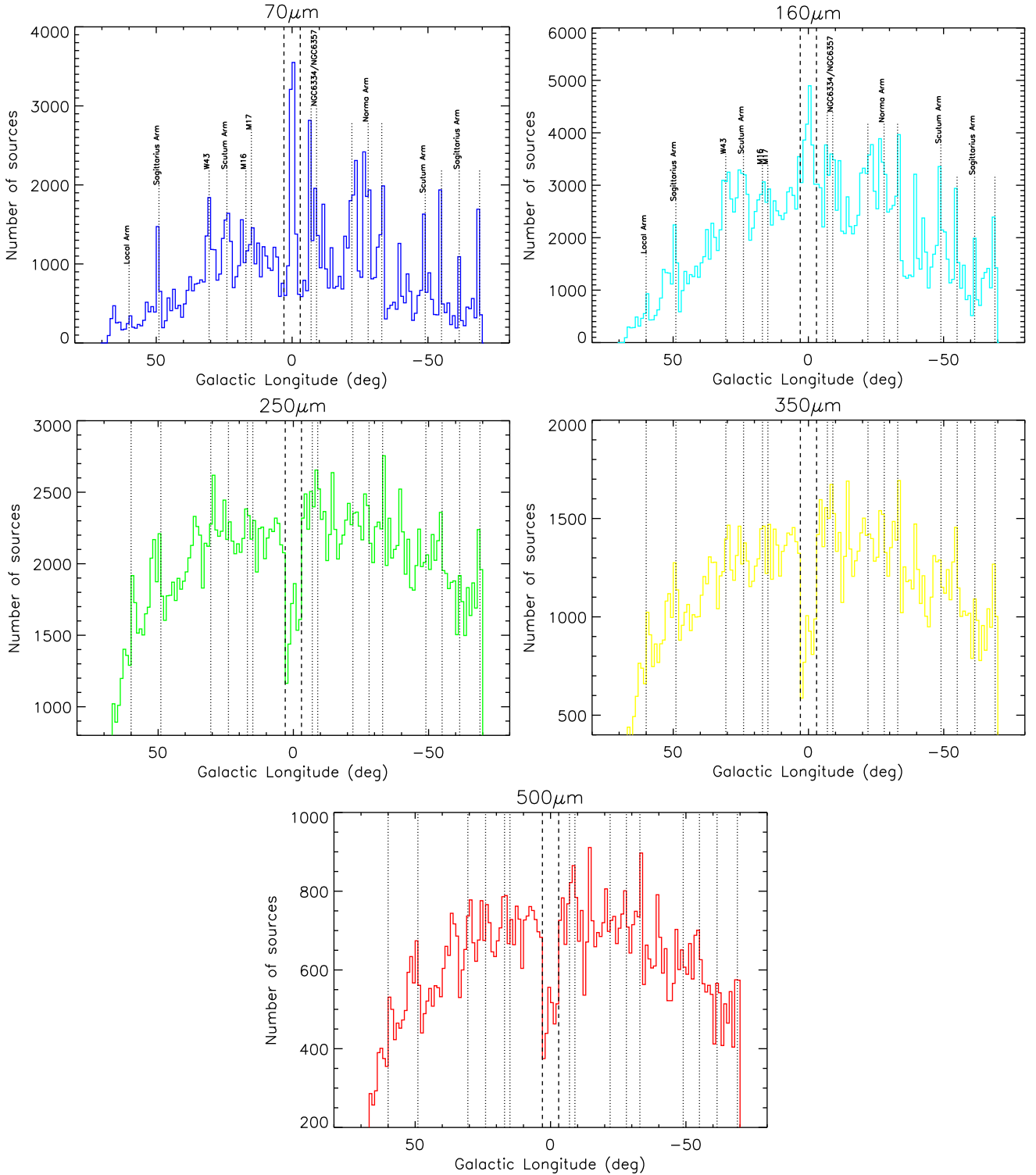


Fig. 20. Longitude distribution of source counts (in 1° bins) at 70, 160, 250, 350, and $500\ \mu\text{m}$ colour-coded as in Fig. 9. The vertical dashed lines denote the longitude range close to the Galactic centre where SPIRE was used in bright-source mode to avoid saturation and non-linearities in detector response. Labelled dotted lines indicate major spiral arms, tangent point/intersections or star-forming complexes.

sources are mildly elliptical, with axis ratios peaking between 1.2 and 1.3, and with the large majority of the sources showing values below 1.5.

It is not surprising to find such a low number of PSF-like sources in the Hi-GAL catalogues. Compact dust clumps around young star-forming objects do not show abrupt transitions in density when they merge with the ISM filaments or clouds in

which they are embedded, so there is no reason a priori to expect these objects to be unresolved. The physical size of dense clumps hosting protoclusters, on average between 0.1 and 1 parsecs, should indeed be resolvable for a large span of heliocentric distances with the angular resolutions accessible to the *Herschel* cameras. This aspect will be discussed in more detail in Elia et al. (in prep.). On the other hand, it has been noted several times

that the intensity of extended emission background in the DR1 Hi-GAL maps is generally higher (Fig. 14) than the peak flux of the detected compact sources. The ideal flat and faint background conditions of the α Boo image that was used in Sect. 4.6 to calibrate the departures of the brightness profile for point-like and mildly extended compact sources are never found on the Galactic plane at *Herschel* wavelengths, with the exception of some spots in the most peripheral tiles at 70 μ m. Under these conditions, it is certainly difficult for any adaptive brightness profile-fitting algorithm to converge to PSF-like source sizes.

6. Global properties of the Galactic structure

Figure 20 shows the distribution of Hi-GAL sources in Galactic longitude for the five wavelength bands. All histograms show decreasing source counts as a function of distance from the Galactic centre, comparing very well with similar plots from other infrared and submillimetre surveys. A variety of peaks can be seen throughout the longitude range, with a greater dynamic range for the 70 and 160 μ m bands. The abrupt dips in source count over the 6°-wide region centred on the Galactic centre that are clearly visible in the SPIRE bands arise because SPIRE was used in bright-source mode for the three tiles of the survey close to the Galactic centre (see Sect. 2).

Similar to Beuther et al. (2012), we identify in Fig. 20 features that can be associated with major star formation complexes or to source accumulations along the line of sight corresponding to tangent points or major intersections of the line of sight with known spiral arms.

A comparison with the ATLASGAL survey (Schuller et al. 2009), covering the Galactic plane between roughly +60° and -60° in the 870 μ m continuum, shows substantial similarities in the source count distributions, confirming that both surveys are mostly tracing dense, star-forming (or potentially star-forming) regions. A similar distribution was also found by Rygl et al. (2010) using high-extinction clouds identified with *Spitzer* colour excess. Therefore it is reasonable to posit that ATLASGAL typically traces the higher flux fraction of the Hi-GAL sources, although this depends on the intrinsic SEDs of the various objects. We defer a detailed analysis of this topic to a subsequent paper (Elia et al., in prep.).

The latitude distribution of the Hi-GAL compact sources is reported in Fig. 21 for the 70 μ m and 250 μ m catalogue sources. Both histograms peak at slightly negative values, similar to what was recently reported for the ATLASGAL submillimetre source distribution and for other infrared and molecular line data Galactic plane surveys (see Beuther et al. 2012 and references therein). The median values for Hi-GAL source latitude is $\sim -0.06^\circ$ below the nominal midplane, in excellent agreement with the value reported for ATLASGAL by Beuther et al. (2012). We therefore confirm that the current definition of the Galactic midplane may need to be revisited to account for a latitude shift that most likely reflects an overall bias, which may be due to an incorrect assumption of the Sun's vertical position in the Milky Way. A deeper and statistically significant analysis of the latitude distribution of the Hi-GAL sources as a function of longitude is deferred to a companion paper (Molinari et al. 2016).

7. Conclusions

This is the first public data release of high-quality products from the *Herschel* Hi-GAL survey. The release comes two years after the end of the *Herschel* observing campaign and is the result

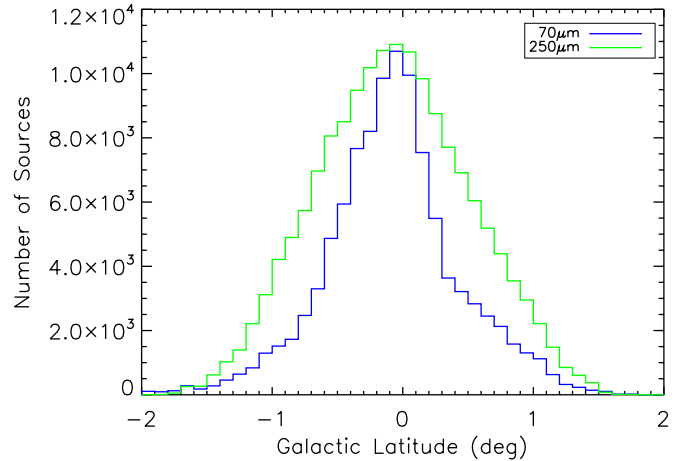


Fig. 21. Distribution of Galactic latitude values for the Hi-GAL sources with $F_{\text{int}} \geq 0.5$ Jy at 70 μ m (blue line), and with $F_{\text{int}} \geq 3.0$ Jy at 250 μ m (green line).

of extensive testing of the data reduction and extraction procedures created by members of the Hi-GAL consortium. The complexity and the large variation of the background conditions in all *Herschel* wavelength bands makes source extraction on the Galactic plane a challenging task. With Hi-GAL DR1, we provide access¹ through a cutout service to high-quality images and compact source catalogues for the Galactic plane at 70, 160, 250, 350, and 500 μ m in the region $68^\circ \geq l \geq -70^\circ$ and $|b| \leq 1^\circ$.

The catalogues were generated using the CuTex software package that was specifically designed to operate in the intense and highly spatially variable background conditions found in the Galactic plane at far-infrared wavelengths. Source detection was carried out on the second derivative of the brightness images, which is particularly sensitive to curvature in the continuum brightness spatial distribution. The detection is optimised for compact objects with FWHM typically ranging from one to three times the instrumental PSF (but mostly within twice the PSF). The effect of false positives was estimated, and a careful analysis of the flux completeness limits was presented separately for each photometric band. The source catalogues contain 123210, 308509, 280685, 160972, and 85460 sources in the five bands.

After considerable time, effort, and experience gathered by using the photometric catalogues by Hi-GAL consortium astronomers, we are not yet at a stage where we can confidently define a figure of merit that can uniquely and definitively be used to assess the degree of reliability of a source detection. Thresholding on the S/N ratio that we assigned to each source appears to be the best way to select bona fide compact objects, although we caution that as a result of the complex background conditions, there may be sources with a formal $S/N < 3$ that have relatively good contrast ratios over the background and appear reliable on visual inspection. An additional criterion to assess the reliability of sources is their persistence in other adjacent photometric bands.

Subsequent releases are planned that will cover the entire Galactic plane, with even higher quality catalogues based on improved handling of the problems present in source extraction for variable-size objects in extreme background conditions. Additional products will include carefully intercalibrated large map mosaics and dust column density maps.

Acknowledgements. We thank an anonymous referee for valuable comments that improved the original manuscript. This work is part of the VIALACTEA Project, a Collaborative Project under Framework Programme 7 of the European Union, funded under Contract # 607380 that is hereby acknowledged. *Herschel* Hi-GAL data processing, maps production and source catalogue generation is the result of a multi-year effort that was initially funded thanks to Contracts I/038/080/0 and I/029/12/0 from ASI, Agenzia Spaziale Italiana. *Herschel* is an ESA space observatory with science instruments provided by European-led Principal Investigator consortia and with important participation from NASA. PACS has been developed by a consortium of institutes led by MPE (Germany) and including UVIE (Austria); KUL, CSL, IMEC (Belgium); CEA, OAMP (France); MPIA (Germany); IAPS, OAP/OAT, OAA/CAISMI, LENS, SISSA (Italy); IAC (Spain). This development has been supported by the funding agencies BMVIT (Austria), ESA-PRODEX (Belgium), CEA/CNES (France), DLR (Germany), ASI (Italy), and CICYT/MCYT (Spain). SPIRE has been developed by a consortium of institutes led by Cardiff Univ. (UK) and including Univ. Lethbridge (Canada); NAOC (China); CEA, LAM (France); IAPS, Univ. Padua (Italy); IAC (Spain); Stockholm Observatory (Sweden); Imperial College London, RAL, UCL-MSSL, UKATC, Univ. Sussex (UK); Caltech, JPL, NHSC, Univ. Colorado (USA). This development has been supported by national funding agencies: CSA (Canada); NAOC (China); CEA, CNES, CNRS (France); ASI (Italy); MCINN (Spain); Stockholm Observatory (Sweden); STFC (UK); and NASA (USA).

References

- Aguirre, J. E., Ginsburg, A. G., Dunham, M. K., et al. 2011, *ApJS*, **192**, 4
- Amores, E. B., Sodré, L., Minniti, D., et al. 2012, *AJ*, **144**, 127
- André, P., Men'shchikov, A., Bontemps, S., et al. 2010, *A&A*, **518**, L102
- Bally, J., Anderson, L. D., Battersby, C., et al. 2010, *A&A*, **518**, L90
- Balog, Z., Müller, T., Nielbock, M., et al. 2014, *Exp. Astr.*, **37**, 129
- Battersby, C., Bally, J., Ginsburg, A., et al. 2011, *A&A*, **535**, A128
- Beltrán, M. T., Olmi, L., Cesaroni, R., et al. 2013, *A&A*, **552**, A21
- Bendo, G., Griffin, M. J., Bock, J. J., et al. 2013, *MNRAS*, **433**, 3062
- Benjamin, R. A., Churchwell, E., Babler, B. L., et al. 2005, *ApJ*, **630**, L149
- Bernard, J. P., Paradis, D., Marshall, D. J., et al. 2010, *A&A*, **518**, L88
- Beuther, H., Tackenberg, J., Linz, H., et al. 2012, *ApJ*, **747**, 43
- Boselli, A., Eales, S., Cortese, L., et al. 2010, *PASP*, **122**, 261
- Burton, M. G., Braiding, G., Glueck, C., et al. 2013, *PASA*, **30**, 44
- Carey, S. J., Noriega-Crespo, A., Mizuno, D. R., et al. 2009, *PASP*, **121**, 76
- Ciesla, L., Boselli, A., Smith, M. W. L., et al. 2012, *A&A*, **543**, A161
- Compiègne, M., Flagey, N., Noriega-Crespo, A., et al. 2010, *ApJ*, **724**, L44
- Compiègne, M., Verstraete, L., Jones, A., et al. 2011, *A&A*, **525**, A103
- Contreras, Y., Schuller, F., Urquhart, J. S., et al. 2013, *A&A*, **549**, A45
- Dempsey, J. T., Thomas, H. S., & Currie, M. J. 2013, *ApJS*, **209**, 8
- Desert, F.-X., Boulanger, F., & Puget, J.-L. 1990, *A&A*, **237**, 215
- Doi, Y., Takita, S., Ootsubo, T., et al. 2016, *PASJ*, **68**, 35
- Eales, S., Dunne, L., Clements, D., et al. 2010, *PASP*, **122**, 499
- Elia, D., Molinari, S., Schisano, E., et al. 2010, *A&A*, **518**, L97
- Elia, D., Molinari, S., Fukui, Y., et al. 2013, *ApJ*, **772**, 45
- Elia, D., Strafella, F., Schneider, N., et al. 2014, *ApJ*, **788**, 3
- Górski, K. M., Hivon, E., Banday, A. J., et al. 2005, *ApJ*, **622**, 759
- Green, J. A., Caswell, J. L., Fuller, G. A., et al. 2012, *MNRAS*, **420**, 3108
- Griffin, M. J., Abergel, A., Abreu, A., et al. 2010, *A&A*, **518**, L3
- Heyer, M. H., Brunt, C., Snell, R. L., et al. 1998, *ApJS*, **115**, 241
- Jackson, J. M., Rathborne, J. M., Shah, R. Y., et al. 2006, *ApJS*, **163**
- Jackson, J. M., Rathborne, J. M., Foster, J. B., et al. 2013, *PASA*, **30**, 57
- Jones, P. A., Burton, M. G., Cunningham, M. R., et al. 2012, *MNRAS*, **419**, 2961
- Kendrew, S., Simpson, R., Bressert, E., et al. 2012, *ApJ*, **755**, 71
- Longmore, S. N., Rathborne, J. M., Bastian, N., et al. 2012, *ApJ*, **746**, L117
- Lucas, P. W., Hoare, M. G., Longmore, A., et al. 2008, *MNRAS*, **391**, 136
- Lutz, D., Poglitsch, A., Altieri, B., et al. 2011, *A&A*, **532**, L12
- Lutz, D., Poglitsch, A., Altieri, B., et al. 2013, *VizieR Online Data Catalog*, **J/A+A/532/A90**
- Marleau, F. R., Noriega-Crespo, A., Paladini, R., et al. 2008, *AJ*, **136**, 662
- McClure-Griffiths, N. M., Green, A. J., Dickey, J. M., et al. 2001, *ApJ*, **551**, 394
- Mizuno, A., & Fukui, Y. 2004, *ASP Conf. Ser.*, **317**, 59
- Molinari, S., Swinyard, B., Bally, J., et al. 2010a, *A&A*, **518**, L100
- Molinari, S., Swinyard, B., Bally, J., et al. 2010b, *PASP*, **122**, 314
- Molinari, S., Bally, J., Noriega-Crespo, A., et al. 2011a, *ApJ*, **735**, L33
- Molinari, S., Schisano, E., Faustini, F., et al. 2011b, *A&A*, **530**, A10
- Molinari, S., Bally, J., Glover, S., et al. 2014, in *Protostars and Planets V*, eds. H. Beuther, R. Klessen, C. P. Dullemond, & T. Henning (University of Arizona Press), 125
- Molinari, S., Bally, J., Noriega-Crespo, A., et al. 2016, *A&A*, **588**, A75
- Moore, T. J. T., Plume, R., Thompson, M. A., et al. 2015, *MNRAS*, **453**, 4264
- Mottram, J. C., & Brunt, C. 2012, *MNRAS*, **420**, 10
- Müller, T., Balog, Z., Nielbock, M., et al. 2014, *Exp. Astron.*, **37**, 253
- Natoli, P., de Gasperis, G., Gheller, C., & Vittorio, N. 2001, *A&A*, **372**, 346
- Ott, S. 2010, in *ASP Conf. Ser.*, *Astronomical Data Analysis Software and System XIX*, eds. M. O. Y. Mizumoto, & K.-I. Morita, 434, 139
- Paladini, R., Umana, G., Veneziani, M., et al. 2012, *ApJ*, **760**, 149
- Paradis, D., Veneziani, M., Noriega-Crespo, A., et al. 2010, *A&A*, **520**, L8
- Paradis, D., Paladini, R., Noriega-Crespo, A., et al. 2012, *A&A*, **537**, A12
- Pezzuto, S., Elia, D., Schisano, E., et al. 2012, *A&A*, **547**, A13
- Piazzo, L., Ikhenade, D., Natoli, P., et al. 2012, *IEEE Transactions on Image Processing*, **21**, 3687
- Pilbratt, G., Riedinger, J. R., Passvogel, T., et al. 2010, *A&A*, **518**, L1
- Planck Collaboration I. 2011, *A&A*, **536**, A1
- Planck Collaboration IX. 2011, *A&A*, **536**, A9
- Poglitsch, A., Waelkens, C., Geis, N., et al. 2010, *A&A*, **518**, L2
- Purcell, C. R., Hoare, M. G., Cotton, W. D., et al. 2013, *ApJS*, **205**, 1
- Rigby, E. E., Maddox, S. J., Dunne, L., et al. 2011, *MNRAS*, **415**, 2336
- Rosolowsky, E., Dunham, M. K., Ginsburg, A., et al. 2010, *ApJS*, **188**, 123
- Rygl, K. L. J., Wyrowski, F., Schuller, F., & Menten, K. M. 2010, *A&A*, **515**, A26
- Sánchez-Portal, M., Marston, A., Altieri, B., et al. 2014, *Exp. Astron.*, **37**, 453
- Schisano, E., Rygl, K. L. J., Molinari, S., et al. 2014, *ApJ*, **791**, 27
- Schuller, F., Menten, K. M., Contreras, Y., et al. 2009, *A&A*, **504**, 415
- SPIRE Instrument Team & Consortium 2014, *SPIRE Handbook*, herschel-doc 0798, v2.5 edn.
- Strafella, F., Lorenzetti, D., Giannini, T., et al. 2015, *ApJ*, **798**, 104
- Thompson, M. A., Urquhart, J. S., Moore, T. J. T., & Morgan, L. K. 2012, *MNRAS*, **421**, 408
- Tibbs, C. T., Paladini, R., Compiègne, M., et al. 2012, *ApJ*, **754**, 94
- Traficante, A., Calzoletti, L., Veneziani, M., et al. 2011, *MNRAS*, **416**, 2932
- Traficante, A., Paladini, R., Compiègne, M., et al. 2014, *MNRAS*, **440**, 3588
- Traficante, A., Fuller, G. A., Peretto, N., Pineda, J. L., & Molinari, S. 2015, *MNRAS*, **451**, 3089
- Umana, G., Ingallinera, A., Trigilio, C., et al. 2012, *MNRAS*, **427**, 2975
- Veneziani, M., Elia, D., Noriega-Crespo, A., et al. 2013, *A&A*, **549**, A8
- Wang, K., Testi, L., Ginsburg, A., et al. 2015, *MNRAS*, **450**, 4043
- Wilcock, L. A., Ward-Thompson, D., Kirk, J. M., et al. 2012, *MNRAS*, **424**, 716
- Wright, E. L., Eisenhardt, P., Mainzer, A. K., et al. 2010, *AJ*, **140**, 1868
- Zavagno, A., Anderson, L. D., Russeil, D., et al. 2010, *A&A*, **518**, L101

¹ INAF–Istituto di Astrofisica e Planetologia Spaziale, via Fosso del Cavaliere 100, 00133 Roma, Italy
e-mail: molinari@iaps.inaf.it

² Jodrell Bank centre for Astrophysics, School of Physics and Astronomy, University of Manchester, Manchester, M13 9PL, UK

³ STFC, Rutherford Appleton Labs, Didcot, OX11 1QX, UK

⁴ Space Telescope Science Institute, 3700 San Martin Dr., Baltimore, 21218 MD, USA

⁵ Centre for Astrophysics and Space Astronomy (CASA), Department of Astrophysical and Planetary Sciences, University of Colorado, Boulder, USA

⁶ Astrophysics Research Institute, Liverpool John Moores University, I22 Liverpool Science Park, 146 Brownlow Hill, Liverpool L3 5RF, UK

⁷ Department of Physics & Astronomy, University of Calgary, Calgary, AB T2N 1N4, Canada

⁸ LAM, Université de Provence, 13013 Marseille, France

⁹ ESA, Directorate of Science, Scientific Support Office, European Space Research and Technology Centre (ESTEC/SCI-S), Keplerlaan 1, 2201 AZ Noordwijk, The Netherlands

¹⁰ Leiden Observatory, Leiden University, PO Box 9513, 2300 RA, Leiden, The Netherlands

¹¹ DIET, Università di Roma “La Sapienza”, 00185 Roma, Italy

¹² Infrared Processing Analysis centre, California Institute of Technology, Pasadena, CA 91125, USA

¹³ Herschel Science centre, ESA/ESAC, PO Box 78, Villanueva de la Cañada, 28691 Madrid, Spain

¹⁴ ASI Science Data centre, 00044 Frascati, Roma, Italy

¹⁵ Dipartimento di Fisica e Scienze della Terra, Università degli Studi di Ferrara e Sezione INFN di Ferrara, via Saragat 1, 44100 Ferrara, Italy

- ¹⁶ Dipartimento di Fisica, Università di Roma “La Sapienza”, P. le Aldo Moro 2, 00138 Roma, Italy
- ¹⁷ Departamento de Fisica, Universidad de Atacama, Copiapó, Chile
- ¹⁸ INAF–Istituto di Radioastronomia, via P. Gobetti 101, 40129 Bologna, Italy
- ¹⁹ Department of Physics and Astronomy, University College London, London, WC1E 6BT, UK
- ²⁰ Université de Toulouse, UPS, CESR, and CNRS, UMR5187, Toulouse, France
- ²¹ CNRS, IRAP, 9 Av. Colonel Roche, BP 44346, 31028 Toulouse Cedex 4, France
- ²² Canadian Institute for Theoretical Astrophysics, University of Toronto, Toronto, ON M5S, Canada
- ²³ European Southern Observatory, Garching bei München, Germany
- ²⁴ INAF–Osservatorio Astrofisico di Arcetri, Firenze, Italy
- ²⁵ Space Science Institute, Boulder, CO, USA
- ²⁶ Laboratoire AIM, CEA/DSM – INSU/CNRS – Université Paris Diderot, IRFU/SaP CEA-Saclay, 91191 Gif-sur-Yvette, France
- ²⁷ Institut de RadioAstronomie Millimétrique (IRAM), Granada, Spain
- ²⁸ Spitzer Science centre, California Institute of Technology, Pasadena, CA 9125, USA
- ²⁹ HYGEOS, Euratechnologies, 165 Avenue de Bretagne, 59000 Lille, France
- ³⁰ Université de Strasbourg, CNRS, UMR 7550, 11 rue de l’Université, 67000 Strasbourg, France
- ³¹ Department of Astrophysics, Nagoya University, 464-8601 Nagoya, Japan
- ³² School of Physics and Astronomy, University of Leeds, Leeds LS2 9JT, UK
- ³³ National Astronomical Observatories, Chinese Academy of Sciences, 100864 Beijing, PR China
- ³⁴ Département de Physique, Université Laval, Québec, QC G1V 0A6, Canada
- ³⁵ The SETI Institute, 189 Bernardo Avenue Suite 100, Mountain View, CA 94043, USA
- ³⁶ School of Physics and Astronomy, Cardiff University, Cardiff, UK
- ³⁷ Max-Planck-Institut für Astronomie, Königstuhl 17, 69117 Heidelberg, Germany
- ³⁸ Physikalisches Institut der Universität zu Köln, Zùlpicher Str. 77, 50937 Köln, Germany
- ³⁹ Univ. Bordeaux, LAB, UMR 5804, CNRS, 33270, Floirac, France
- ⁴⁰ SRON Netherlands Institute for Space Research, Zernike Building, PO Box 800, 9700 AV Groningen, The Netherlands
- ⁴¹ Dipartimento di Matematica e Fisica, Università del Salento, Lecce, Italy
- ⁴² Centre for Astrophysics Research, Science and Technology Research Institute, University of Hertfordshire, Hatfield AL10 9AB, UK
- ⁴³ INAF–Osservatorio Astrofisico di Catania, Catania, Italy
- ⁴⁴ Jeremiah Horrocks Institute, University of Central Lancashire, Preston PR1 2HE, UK
- ⁴⁵ Max-Planck-Institut für Radioastronomie (MPIfR), 53121 Bonn, Germany

Appendix A: Explanatory note for the Hi-GAL photometric catalogues

Table A.1. Field description for the single-band photometric catalogs.

Field name	Format	Units	Description
Source identification and position information			
DESIGNATION	A25	–	Designation of the source based on its Galactic position in the form LLL.Llll±b.bbbb. The naming convention for the Hi-GAL catalogue has the form HIGALPXLLL.Llll±b.bbbb, where HIGALP stands for the preliminary catalogue, X stands for the band where the source has been identified among the possible choices: B – blue band; R – red band; S – PSW band; M – PMW band; L – PLW band.
GLON	F12.6	degrees	Galactic longitude of the source.
GLAT	F12.6	degrees	Galactic latitude of the source.
DGLON	F5.2	arcsec	Uncertainty in the Galactic longitude coordinate derived from the fitting procedure. 0 indicates that the fitting process hit the boundary limits imposed on the fit.
DGLAT	F5.2	arcsec	Uncertainty in the Galactic latitude coordinate derived from the fitting procedure. 0 indicates that the fitting process hit the boundary limits imposed on the fit.
RA	F12.6	degrees	J2000 Right Ascension of the source.
DEC	F12.6	degrees	J2000 Declination of the source.
ATLAS_IMAGE	A40	–	Atlas image file identifier from which the source was extracted.
X	F9.3	pixel	x -pixel coordinate of this source in the original image.
Y	F9.3	pixel	y -pixel coordinate of this source in the original image.
DX	F9.3	pixel	Uncertainty in the x coordinate of this source derived from the fitting procedure.
DY	F9.3	pixel	Uncertainty in the y coordinate of this source derived from the fitting procedure.
SOURCE_ID	A10	–	Unique source identification in the form ILLL NNNN, where ILLL is a unique identifier of the original image over which source extraction was carried out, and NNNN is a progressive four-digit, zero-filled number indicating the sequential order of extraction.
Primary photometric information			
FINT_UNCORR	F15.3	Jy	Source-integrated flux measured from the fitting process.
FINT	F15.3	Jy	Source-integrated flux measured from the fitting process after applying photometric corrections as a function of the source size, to account for source non-Gaussianity and for scan speed.
ERR_FINT	F15.3	Jy	Uncertainty on the integrated flux computed by multiplying the fitted source residual rms (RMS_TOTAL) by the fitted source area as estimated by FWHMA and FWHMB.
FPEAK	F15.3	MJy/sr	Source peak flux measured from the fitting process.
FWHMA	F10.2	arcsec	Full width at half maximum of the source along axis a of the elliptical Gaussian as determined by fitting engine.
FWHMB	F10.2	arcsec	Full width at half maximum of the source along axis b of the elliptical Gaussian as determined by fitting engine.
PA	F6.1	degrees	Position angle of the elliptical Gaussian (N→E).
BACKGROUND	F15.3	MJy/sr	Background value determined at the source peak position.
BACK_ACOEFF	F12.5	MJy/sr	Coefficient a of the zero-order term of the background obtained by the fit at the source peak position.
BACK_BCOEFF	F12.5	MJy/sr/pxl	Coefficient b of the first-order term x of the background obtained by the fit at the source peak position.
BACK_CCOEFF	F12.5	MJy/sr/pxl	Coefficient c of the first-order term y of the background obtained by the fit at the source peak position.
BACK_DCOEFF	F12.5	MJy/sr/pxl ²	Coefficient d of the second-order term x^2 of the background obtained by the fit at the source peak position.
BACK_ECOEFF	F12.5	MJy/sr/pxl ²	Coefficient e of the second-order term y^2 of the background obtained by the fit at the source peak position.
BACK_FCOEFF	F12.5	MJy/sr/pxl ²	Coefficient f of the second-order term xy of the background obtained by the fit at the source peak position.
RMS_TOTAL	F12.5	MJy/sr	Standard deviation, σ_{loc} , of the residuals computed within the source area defined by FWHMA and FWHMB after subtracting the best fit.
RMS_SURROUND	F12.5	MJy/sr	Standard deviation, σ_{loc} , of the residuals computed within the fitting window after subtracting the best fit, excluding both the pixels that belong to the source and the pixels belonging to other sources that fall within the fitting window.
SNR	F12.5	–	Signal-to-noise ratio obtained by dividing FPEAK by the residual rms over a source area with FWHMA and FWHMB as <i>semi-axes</i> .
Basic detection information			
DET_X	F10.3	–	Relevance of the source in the second-derivative map along the x -axis defined as the ratio between the measured second derivative at source peak position and the adopted local threshold value.
DET_Y	F10.3	–	Relevance of the source in the second-derivative map along the y -axis defined as the ratio between the measured second derivative at source peak position and the adopted local threshold value.

Table A.1. continued.

Field name	Format	Units	Description
Basic extraction information			
DET_X45	F10.3	–	Relevance of the source in the second-derivative map along the bisector of the xy -axis defined as the ratio between the measured second derivative at source peak position and the adopted local threshold value.
DET_Y45	F10.3	–	Relevance of the source in the second-derivative map along the bisector of the yx -axis defined as the ratio between the measured second derivative at source peak position and the adopted local threshold value.
DETLIM_X	F10.3	MJy/sr/pxl ²	Absolute value for the local detection limit threshold adopted for the second derivative along the x -axis coordinate.
DETLIM_Y	F10.3	MJy/sr/pxl ²	Absolute value for the local detection limit threshold adopted for the second derivative along the y -axis coordinate.
DETLIM_X45	F10.3	MJy/sr/pxl ²	Absolute value for the local detection limit threshold adopted for the second derivative along the bisector of the first and third quadrant.
DETLIM_Y45	F10.3	MJy/sr/pxl ²	Absolute value for the local detection limit threshold adopted for the second derivative along the bisector of the second and fourth quadrant.
CLUMP_FLAG	I5	–	Flag for confusion at detection level. A value equal to 0 means that the source was identified from an isolated group of pixels above the threshold in all the four derivative directions. Sources belonging to the extraction of the same atlas image having the same value of this flag belong to the same group of pixels above the threshold.
NCOMP	I2	–	Number of Gaussian components used simultaneously in the fitting process. This number includes the source, so the minimum value is 1, this number is greater than 1 if the source is fit with other nearby detections.
XCENT	F9.1	pxl	The x -pixel coordinate of the centre of the source fitting window in the original image.
YCENT	F9.1	pxl	The y -pixel coordinate of the centre of the source fitting window in the original image.
XWINDOW	I2	pxl	Half-width size of the source fitting window along x coordinate and centred at XCENT.
YWINDOW	I2	pxl	Half-width size of the source fitting window along y coordinate and centred at YCENT.
NCONTAM	I2	–	Number of other sources falling inside the fitting window whose presence is taken into account at fitting stage. Not all those other sources might have been fitted at the same time.
CENT_TOL	F5.2	pxl	Maximum variation in pixels for adjustment of the fit centre with respect to the position of detection, measured as the distance between the latter and the brightest local (within three pixels) pixel in the fitting window.
DOF	I4	–	Degrees of freedom of the source Gaussian fit.
Quality flags			
CHI2	F12.5	–	χ^2 determined by the fitting engine.
CHI2_OPP	F12.5	–	Estimator of the fidelity between the fit and the data computed as $\phi = (O(i) - F(i))^2 / F(i)$, where $O(i)$ is the observed data in the i pixel of the fitting window and $F(i)$ is the fitted value in the same position.
FIT_STATUS	I1	–	Flag returned from the fitting engine. Possible values of the flag are: 0 – fit convergence failed; 1 – convergence reached; 2 – convergence reached despite the initial accuracy requested to fitting engine was set too low; 3 – maximum number of iterations in the fitting process reached; 4 – problems in fitting due to the initial guess.
GUESS_FLAG	A3	–	Flag on quality of guessed source parameters as determined at the detection stage. The form of the flag is GN, where G is a letter defined as A – optimal number of positions to estimate the size; B – sufficient number of positions to estimate the size; C – low number of positions to estimate the size; and N is a number defining the quality of initial guess size: 0 – initial estimate failed; 1 – good initial estimate for sizes; 2 – one of the two guessed sizes was initially estimate as smaller than the PSF; 3 – initial estimates of source sizes were higher than three times the PSF.
GROUP_FLAG	I5	–	Flag on quality of guessed source parameters as determined at the detection stage. The form of the flag is GN, where G is a letter defined as A – optimal number of positions to estimate the size; B – sufficient number of positions to estimate the size; C – low number of positions to estimate the size; and N is a number defining the quality of initial guess size: 0 – initial estimate failed; 1 – good initial estimate for sizes; 2 – one of the two guessed sizes was initially estimated as smaller than the PSF; 3 – initial estimates of source sizes were higher than three times the PSF.
CONSTRAINTS	I1	–	Flag indicating the number of parameters that reached the tolerance limits allowed to the fit process. Values of 4 indicate that the source flux has higher unreliability since either the centre and its sizes have reached the maximum (or the minimum) allowed for the fit engine.
SHIFT_FLAG	F9.3	arcsec	Amount of shift of the source peak position from its original detection position, due to Gaussian fitting.

Table A.1. continued.

Field name	Format	Units	Description
Basic extraction information			
RDETP2DX	F9.3	–	Ratio between the second-derivative value along x direction expected by the fitted model of the source and the second derivative derivative measured at the detection stage. Values closer to one indicate a higher reliability of the source.
RDETP2DY	F9.3	–	Ratio between the second-derivative value along y direction expected by the fitted model of the source and the second derivative measured at the detection stage. Values closer to one indicate a higher reliability of the source.
RDETP2DX45	F9.3	–	Ratio between the second-derivative value along the bisector of the xy direction expected by the fitted model of the source and the second derivative measured at the detection stage. Values closer to one indicate a higher reliability of the source.
RDETP2DY45	F9.3	–	Ratio between the second-derivative value along the bisector of the yx direction expected by the fitted model of the source and the second derivative measured at the detection stage. Values closer to one indicate a higher reliability of the source.
OVERLAP_FLAG	F9.3	–	Flag to indicate whether the source has been detected and extracted in one or more adjacent tiles. H indicates that the source has been detected in the tile named in column ATLAS_IMAGE; E,W indicate that the source is detected only in the eastern or western adjacent tile, respectively (east is higher Galactic longitude); if the source has been detected in both H and E or W, then the name of the adjacent tile is also listed (e.g. H_l060). In these cases, the entry in the catalogue is the one with the highest S/N.
OVFLUX_FLAG	I	–	Flag to indicate which flux values were adopted if detected and extracted in two adjacent tiles. 0 indicates that the source has been detected only once and therefore all fluxes refer to this detection. –1 indicates that the two fluxes differ by more than 15%; the one listed is that with the highest S/N. 1 indicates that both integrated fluxes lie within 15%, the one in the catalogue is that with the highest S/N. 2 indicates that the integrated fluxes differ by more than 15% but FPEAK are within 15%; the one listed is that with the highest S/N.

Appendix B: Saturated pixels in Hi-GAL maps

Table B.1 reports the location of the clusters of saturated pixels in the Hi-GAL mapped area. The longitudes and latitudes in Cols. 1–2 represent the centroid position of the cluster at the shortest wavelength where the saturation conditions exists. The subsequent eight columns report for each band from 160

to 500 μm the number of saturated pixels for each location and the radius of the circularised area of the saturated pixels cluster in arcseconds. The last column reports the sources from the IRAS Point Source Catalogue or from the RMS Source Catalogue that are located within 1' (for IRAS sources) and 40'' (for MSX sources) from the pixels cluster centroid.

Table B.1. Clumps or clusters of saturated pixels, crossmatched with IRAS point sources and rms sources. IRAS sources $<60''$, rms sources $<40''$ from the cluster barycentre.

Gal. Lon. ($^{\circ}$)	Gal. Lat. ($^{\circ}$)	Map	Red		PSW		PMW		PLW		IRAS	rms
			Pix.	R_e ($''$)	Pix.	R_e ($''$)	Pix.	R_e ($''$)	Pix.	R_e ($''$)		
291.26944	-0.71532	1290	-	-	67	27	1	4	-	-	11 097-6102	-
291.57932	-0.43251	1290	-	-	7	8	-	-	-	-	-	G291.5765-00.4310
291.26944	-0.71508	1292	-	-	67	27	3	7	-	-	11 097-6102	-
291.57941	-0.43112	1292	-	-	4	6	-	-	-	-	-	G291.5765-00.4310
301.13687	-0.22566	1301	-	-	18	14	3	7	-	-	12 326-6245	G301.1364-00.2249
305.20917	0.20578	1305	-	-	8	9	-	-	-	-	13 079-6218	G305.2017+00.2072A, G305.2017+00.2072B
305.35797	0.20391	1305	-	-	6	8	-	-	-	-	13 092-6218	-
305.36215	0.15114	1305	-	-	3	5	-	-	-	-	-	-
305.36771	0.21224	1305	-	-	1	3	-	-	-	-	-	G305.3676+00.2095, G305.3779+00.2108
305.79990	-0.24385	1305	-	-	3	5	-	-	-	-	13 134-6242	G305.7991-00.2461A, G305.7991-00.2461B
309.92188	0.47956	1310	-	-	2	4	-	-	-	-	13 471-6120	G309.9206+00.4790A, G309.9206+00.4790B
311.62744	0.29010	1312	-	-	5	7	-	-	-	-	14 013-6105	G311.6264+00.2897
314.21927	0.27282	1314	-	-	1	3	-	-	-	-	14 214-6017	G314.2204+00.2726
316.81213	-0.05743	1316	-	-	3	5	-	-	-	-	14 416-5937	G316.8112-00.0566
318.04984	0.08687	1319	-	-	1	3	-	-	-	-	14 498-5856	G318.0489+00.0854A, G318.0489+00.0854B, G318.0489+00.0854C
318.94812	-0.19645	1319	-	-	1	3	-	-	-	-	-	G318.9480-00.1969A, G318.9480-00.1969B
322.15808	0.63623	1321	-	-	23	16	4	9	-	-	-	-
322.16376	0.62281	1321	-	-	13	12	-	-	-	-	-	-
322.15823	0.63590	1323	-	-	21	15	-	-	-	-	-	-
322.16400	0.62258	1323	-	-	7	8	-	-	-	-	-	-
323.74069	-0.26362	1323	-	-	5	7	-	-	-	-	15 278-5620	G323.7399-00.2617A, G323.7399-00.2617B, G323.7410-00.2552A, G323.7410-00.2552B, G323.7410-00.2552C
324.20078	0.12143	1323	-	-	6	8	-	-	-	-	15 290-5546	G324.1997+00.1192
324.20093	0.12056	1325	-	-	5	7	-	-	-	-	15 290-5546	G324.1997+00.1192
326.47467	0.70227	1325	-	-	4	6	-	-	-	-	15 394-5358	G326.4755+00.6947
326.65701	0.59368	1325	-	-	5	7	-	-	-	-	15 408-5356	-
326.72165	0.61432	1325	-	-	1	3	-	-	-	-	15 411-5352	G326.7249+00.6159A, G326.7249+00.6159B
326.65836	0.59550	1327	-	-	1	3	-	-	-	-	15 408-5356	-
326.67001	0.55551	1327	-	-	1	3	-	-	-	-	-	G326.6687+00.5495
326.72278	0.61440	1327	-	-	3	5	-	-	-	-	15 411-5352	G326.7249+00.6159A, G326.7249+00.6159B
327.29385	-0.57797	1327	-	-	38	20	17	18	3	11	-	G327.2852-00.5735
327.30011	-0.54923	1327	-	-	30	18	-	-	-	-	15 492-5426	-
327.30661	-0.54101	1327	-	-	1	3	-	-	-	-	15 492-5426	-
327.40240	0.44477	1327	-	-	4	6	-	-	-	-	15 454-5335	G327.4014+00.4454
328.23657	-0.54683	1327	-	-	2	4	-	-	-	-	-	-

Table B.1. continued.

Gal. Lon. (°)	Gal. Lat. (°)	Map	Red		PSW		PMW		PLW		IRAS	rms	
			Pix.	R _e (")	Pix.	R _e (")	Pix.	R _e (")	Pix.	R _e (")			
328.25488	-0.53147	1327	-	-	7	8	-	-	-	-	15 541-5349	G328.2523-00.5320A, G328.2523-00.5320C G328.3067+00.4308	G328.2523-00.5320B,
328.30728	0.43178	1327	-	-	7	8	-	-	-	-	15 502-5302		
328.56671	-0.53409	1327	-	-	9	10	-	-	-	-	15 557-5337		
328.57483	-0.53013	1327	-	-	2	4	-	-	-	-	15 557-5337		
328.80792	0.63265	1327	2	3	32	19	8	12	-	-	15 520-5234		
328.57144	-0.53254	1330	-	-	16	13	-	-	-	-	15 557-5337		
328.80875	0.63335	1330	-	-	29	18	7	11	-	-	15 520-5234		
329.02948	-0.20541	1330	-	-	3	5	-	-	-	-	15 566-5304		
329.18417	-0.31345	1330	-	-	2	4	-	-	-	-	15 579-5303		
329.33844	0.14789	1330	-	-	12	11	-	-	-	-	15 567-5236		
329.40497	-0.45928	1330	-	-	1	3	-	-	-	-	15 596-5301		
330.87857	-0.36690	1330	-	-	18	14	3	7	-	-	16 065-5158		G330.8708-00.3715A, G330.8708-00.3715B,
330.95459	-0.18134	1330	7	6	32	19	13	16	-	-	16 060-5146		
330.87854	-0.36711	1332	-	-	19	14	2	6	-	-	16 065-5158		G330.8708-00.3715A,
330.95401	-0.18147	1332	-	-	33	19	12	15	-	-	16 060-5146		
331.13147	-0.24311	1332	-	-	7	8	-	-	-	-	16 071-5142		
331.27811	-0.18765	1332	-	-	1	3	-	-	-	-	16 076-5134		
331.51184	-0.10189	1332	-	-	15	13	-	-	-	-	-		G331.5180-00.0947A,
331.55585	-0.12044	1332	-	-	3	5	-	-	-	-	16 086-5119		
332.09387	-0.42099	1332	-	-	2	4	-	-	-	-	16 124-5110		
332.82730	-0.54833	1332	5	5	33	19	10	14	-	-	16 164-5046		G332.8256-00.5498A, G332.8256-00.5498B
332.96378	-0.67754	1332	-	-	2	4	-	-	-	-	16 175-5045		
333.06830	-0.44629	1332	-	-	9	10	-	-	-	-	-		
333.12161	-0.43240	1332	-	-	9	10	-	-	-	-	16 172-5028		G333.1256-00.4367, G333.1306-00.4275
333.13354	-0.43052	1332	-	-	85	31	14	16	-	-	16 172-5028		G333.1306-00.4275, G333.1256-00.4367
333.28455	-0.38667	1332	-	-	37	20	1	4	-	-	-		G333.2880-00.3907
333.29950	-0.35258	1332	-	-	1	3	-	-	-	-	16 177-5018		
332.82697	-0.54870	1334	-	-	31	18	9	13	1	6	16 164-5046		G332.8256-00.5498A, G332.8256-00.5498B
332.96283	-0.67861	1334	-	-	2	4	-	-	-	-	16 175-5045		
333.06778	-0.44717	1334	-	-	16	13	-	-	-	-	-		
333.12073	-0.43279	1334	-	-	7	8	-	-	-	-	16 172-5028		
333.12357	-0.42208	1334	-	-	1	3	-	-	-	-	16 172-5028		
333.13281	-0.43099	1334	-	-	85	31	18	19	1	6	16 172-5028		G333.1306-00.4275, G333.1256-00.4367
333.28406	-0.38753	1334	-	-	36	20	1	4	-	-	-		G333.2880-00.3907

Table B.1. continued.

Gal. Lon. (°)	Gal. Lat. (°)	Map	Red		PSW		PMW		PLW		IRAS	rms
			Pix.	R _e (")	Pix.	R _e (")	Pix.	R _e (")	Pix.	R _e (")		
333.46677	-0.16383	1334	-	-	3	5	-	-	-	-	16 175-5002	-
333.60181	-0.21256	1334	8	7	93	32	18	19	-	-	16 183-4958	G333.6032-00.2184
333.60635	-0.21475	1334	2	3	93	32	18	19	-	-	16 183-4958	G333.6032-00.2184
333.61011	-0.21475	1334	2	3	93	32	18	19	-	-	16 183-4958	G333.6032-00.2184
335.58456	-0.28968	1336	-	-	5	7	-	-	-	-	16 272-4837	-
335.78864	0.17434	1336	-	-	3	5	-	-	-	-	-	-
336.01752	-0.82527	1336	-	-	1	3	-	-	-	-	16 313-4840	-
336.99533	-0.02706	1336	-	-	7	8	-	-	-	-	16 318-4724	G336.9920-00.0244
337.12134	-0.17316	1336	-	-	3	5	-	-	-	-	16 330-4725	-
337.40457	-0.40154	1336	-	-	22	15	4	9	-	-	16 351-4722	G337.4032-00.4037, G337.4050-00.4071A, G337.4050-00.4071B, G337.4050-00.4071C
337.70480	-0.05338	1336	-	-	10	10	-	-	-	-	16 348-4654	G337.7051-00.0575B
337.71286	0.08847	1336	-	-	3	5	-	-	-	-	16 343-4648	G337.7091+00.0932A, G337.7091+00.0932B, G337.7091+00.0932C
337.40515	-0.40158	1338	-	-	24	16	4	9	-	-	16 351-4722	G337.4032-00.4037, G337.4050-00.4071A, G337.4050-00.4071B
337.70502	-0.05350	1338	-	-	6	8	-	-	1	6	16 348-4654	G337.7051-00.0575B
337.71362	0.08732	1338	-	-	2	4	-	-	-	-	16 343-4648	G337.7091+00.0932A, G337.7091+00.0932B, G337.7091+00.0932C
337.91513	-0.47671	1338	-	-	26	17	5	10	-	-	16 374-4701	-
337.92151	-0.45594	1338	-	-	4	6	-	-	-	-	16 374-4701	G337.9266-00.4588
338.07437	0.00983	1338	-	-	1	3	-	-	-	-	16 359-4635	G338.0715+00.0126A, G338.0715+00.0126B, G338.0715+00.0126C
338.92065	0.55064	1338	-	-	1	3	30	24	-	-	-	G338.9196+00.5495
340.05484	-0.24336	1341	-	-	16	13	-	-	-	-	16 445-4516	G340.0543-00.2437A, G340.0543-00.2437C
340.97015	-1.02083	1341	-	-	2	4	-	-	-	-	16 513-4504	-
343.12711	-0.06283	1343	-	-	22	15	2	6	-	-	16 547-4247	G343.1261-00.0623
343.75632	-0.16335	1343	-	-	2	4	-	-	-	-	16 572-4221	-
344.22766	-0.56794	1343	-	-	10	10	1	4	-	-	-	-
344.22128	-0.59246	1343	-	-	1	3	-	-	-	-	17 006-4215	G344.2207-00.5953
344.22733	-0.56887	1345	-	-	7	8	1	4	-	-	-	-
345.00293	-0.22400	1345	-	-	15	13	1	4	-	-	17 016-4124	G345.0034-00.2240A, G345.0034-00.2240B
345.40417	-0.94387	1345	-	-	2	4	-	-	-	-	17 059-4132	-
345.40503	-0.94054	1345	-	-	1	3	-	-	-	-	17 059-4132	-
345.40759	-0.95251	1345	-	-	11	11	-	-	-	-	17 059-4132	-
345.48730	0.31525	1345	-	-	27	17	2	6	-	-	17 009-4042	G345.4881+00.3148
345.50470	0.34849	1345	-	-	10	10	-	-	-	-	17 008-4040	G345.5043+00.3480

Table B.1. continued.

Gal. Lon. (°)	Gal. Lat. (°)	Map	Red		PSW		PMW		PLW		rms
			Pix.	R _e (")	Pix.	R _e (")	Pix.	R _e (")	Pix.	R _e (")	
345.64835	0.01016	1345	–	–	2	4	–	–	–	–	G345.6495+00.0084
347.62949	0.14830	1347	–	–	1	3	–	–	–	–	–
348.18448	0.48243	1347	–	–	2	4	–	–	–	–	–
348.54904	−0.97985	1349	–	–	8	9	–	–	–	–	–
348.69720	−1.02824	1349	–	–	18	14	1	4	–	–	G348.6972−01.0263
348.70135	−1.04115	1349	–	–	11	11	–	–	–	–	–
348.72681	−1.03991	1349	–	–	36	20	8	12	–	–	G348.7250−01.0435, G348.7342−01.0359B
349.09204	0.10544	1349	–	–	2	4	–	–	–	–	–
350.01199	−1.34354	1349	–	–	1	3	–	–	–	–	–
350.10364	0.08211	1349	–	–	2	4	–	–	–	–	–
350.11032	0.08795	1349	–	–	1	3	–	–	–	–	–
350.11282	0.09461	1349	–	–	2	4	–	–	–	–	–
350.50192	0.95693	1349	–	–	2	4	–	–	–	–	–
350.50858	0.95776	1349	–	–	3	5	–	–	–	–	–
351.15857	0.70003	1349	–	–	67	27	14	16	1	6	–
351.24503	0.66776	1349	–	–	67	27	8	12	–	–	–
351.25070	0.65370	1349	–	–	22	15	–	–	–	–	–
351.15891	0.69968	1352	–	–	58	25	12	15	–	–	–
351.24637	0.66349	1352	–	–	84	31	7	11	–	–	–
351.41672	0.64628	1352	5	5	109	35	22	21	1	6	–
351.44254	0.65746	1352	–	–	97	33	34	26	5	14	–
351.58179	−0.35232	1352	–	–	27	17	8	12	1	6	–
351.62717	−1.26058	1352	–	–	1	3	41	28	2	9	–
351.77597	−0.53590	1352	1	2	46	22	15	17	–	–	–
353.19455	0.90645	1352	–	–	1	3	–	–	–	–	–
353.41052	−0.35994	1354	–	–	22	15	5	10	–	–	–
0.65762	−0.04104	1000	3	4	–	–	–	–	–	–	–
0.66608	−0.03508	1000	30	13	1	3	–	–	–	–	–
0.67696	−0.02762	1000	5	5	–	–	–	–	–	–	–
3.43932	−0.34878	1004	–	–	4	6	–	–	–	–	–
5.88571	−0.39286	1006	3	4	28	17	5	10	–	–	–
5.90034	−0.42896	1006	–	–	4	6	–	–	–	–	–
8.13747	0.22342	1006	–	–	1	3	–	–	–	–	–
8.14080	0.22092	1006	–	–	2	4	–	–	–	–	–
8.66965	−0.35544	1008	–	–	19	14	2	6	–	–	–
9.62041	0.19508	1008	–	–	14	12	1	4	–	–	–
											17 028-4045
											17 167-3854
											17 130-3756
											17 216-3801
											17 160-3707
											17 160-3707
											17 160-3707
											17 136-3617
											17 136-3617
											17 165-3554
											–
											–
											17 165-3554
											–
											–
											17 175-3544
											–
											17 220-3609
											17 258-3637
											17 233-3606
											–
											17 271-3439
											17 441-2822
											17 441-2822
											17 441-2822
											17 517-2609
											17 574-2403
											–
											17 599-2148
											17 599-2148
											18 032-2137
											18 032-2032

Table B.1. continued.

Gal. Lon. (°)	Gal. Lat. (°)	Map	Red		PSW		PMW		PLW		IRAS	rms
			Pix.	R _e (")	Pix.	R _e (")	Pix.	R _e (")	Pix.	R _e (")		
10.29660	-0.14639	1011	-	-	1	3	-	-	-	-	-	-
10.30060	-0.14606	1011	-	-	5	7	-	-	-	-	18 060-2005	-
10.47293	0.02776	1011	-	-	16	13	5	10	-	-	18 056-1952	G010.4718+00.0256, G010.4718+00.0206
10.62483	-0.38273	1011	4	5	42	21	13	16	-	-	18 075-1956	G010.6235-00.3834, G010.6260-00.3744, G010.6311-00.3864 G011.9373-00.6165
11.93718	-0.61500	1011	-	-	5	7	-	-	-	-	18 110-1854	-
12.20841	-0.10072	1011	-	-	5	7	-	-	-	-	18 097-1825A	-
11.93764	-0.61586	1013	-	-	9	10	-	-	-	-	18 110-1854	G011.9373-00.6165
12.20885	-0.10139	1013	-	-	9	10	-	-	-	-	18 097-1825A	-
12.41826	0.50535	1013	-	-	1	3	-	-	-	-	18 079-1756	-
12.80578	-0.19902	1013	6	6	154	42	39	28	2	9	-	G012.8062-00.1987
12.88957	0.48929	1013	-	-	6	8	-	-	-	-	18 089-1732	G012.8909+00.4938A, G012.8909+00.4938B, G012.8909+00.4938C
12.90789	-0.25941	1013	-	-	12	11	-	-	-	-	18 117-1753	G012.9090-00.2607
14.33189	-0.64444	1013	-	-	7	8	-	-	-	-	18 159-1648	G014.3313-00.6397
14.33213	-0.64354	1015	-	-	7	8	-	-	-	-	18 159-1648	G014.3313-00.6397
15.01485	-0.70673	1015	-	-	1	3	-	-	-	-	-	-
15.01896	-0.67179	1015	-	-	315	60	36	27	1	6	18 174-1612	-
17.63897	0.15421	1017	-	-	1	3	-	-	-	-	18 196-1331	G017.6380+00.1566
19.07808	-0.28641	1019	-	-	1	3	-	-	-	-	18 239-1228	G019.0741-00.2861
19.60909	-0.23325	1019	-	-	11	11	-	-	-	-	18 248-1158	G019.6085-00.2357
20.08053	-0.13477	1019	-	-	4	6	-	-	-	-	18 253-1130	G020.0801-00.1360, G020.0722-00.1419
23.20654	-0.37680	1024	-	-	1	3	-	-	-	-	-	-
24.32809	0.14480	1024	-	-	1	3	-	-	-	-	18 324-0737	-
24.79058	0.08432	1024	-	-	14	12	-	-	-	-	-	G024.7891+00.0846
25.64959	1.04886	1026	-	-	5	7	-	-	-	-	18 316-0602	G025.6498+01.0491
25.82551	-0.17718	1026	-	-	1	3	-	-	-	-	-	-
26.51048	0.28280	1026	-	-	1	3	-	-	-	-	18 360-0537	G026.5107+00.2824A, G026.5107+00.2824B, G026.5107+00.2824C
27.36542	-0.16550	1026	-	-	1	3	-	-	-	-	18 391-0504	-
27.36667	-0.16609	1028	-	-	1	3	-	-	-	-	18 391-0504	-
28.19999	-0.04926	1028	-	-	8	9	-	-	-	-	18 403-0417	G028.2007-00.0494A, G028.2007-00.0494B
29.95521	-0.01511	1028	-	-	13	12	-	-	-	-	18 434-0242	G029.9564-00.0174
29.95584	-0.01561	1030	-	-	10	10	-	-	-	-	18 434-0242	G029.9564-00.0174
30.70293	-0.06791	1030	-	-	16	13	1	4	-	-	-	-
30.71995	-0.08227	1030	-	-	5	7	-	-	-	-	-	G030.7206-00.0826
30.81767	-0.05530	1030	-	-	21	15	4	9	-	-	-	-

Table B.1. continued.

Gal. Lon. (°)	Gal. Lat. (°)	Map	Red		PSW		PMW		PLW		rms
			Pix.	R _e (")	Pix.	R _e (")	Pix.	R _e (")	Pix.	R _e (")	
30.81573	-0.05528	1031	-	-	13	12	4	9	-	-	-
31.28092	0.06224	1031	-	-	2	4	-	-	-	-	G031.2803+00.0615A, G031.2803+00.0615B
31.41228	0.30732	1031	-	-	11	11	-	-	-	-	G031.4134+00.3092
32.79803	0.19142	1033	-	-	10	10	-	-	-	-	G032.7977+00.1903
33.91713	0.11108	1033	-	-	1	3	-	-	-	-	G033.9148+00.1093
34.25706	0.15616	1033	-	-	82	30	18	19	3	11	-
34.41228	0.23503	1033	-	-	5	7	-	-	-	-	-
34.25696	0.15447	1035	3	4	75	29	19	19	2	9	-
34.41156	0.23619	1035	-	-	1	3	-	-	-	-	-
35.19689	-0.74271	1035	-	-	8	9	-	-	-	-	G035.1979-00.7427
43.16719	0.01141	1041	29	13	-	-	-	-	-	-	G043.1679+00.0095
43.16536	-0.02749	1044	-	-	7	8	-	-	-	-	G043.1650-00.0285
43.16829	0.01070	1044	9	7	86	31	23	21	2	9	G043.1679+00.0095
43.79532	-0.12582	1044	-	-	1	3	-	-	-	-	G043.7955-00.1275
45.07181	0.13207	1044	-	-	4	6	-	-	-	-	G045.0711+00.1325
45.12346	0.13248	1044	-	-	1	3	-	-	-	-	G045.1221+00.1323
45.07174	0.13254	1046	-	-	3	5	-	-	-	-	G045.0711+00.1325
49.36889	-0.29932	1048	-	-	1	3	-	-	-	-	G049.3697-00.3031
49.48889	-0.38775	1048	6	6	313	59	50	31	7	17	G049.4885-00.3799
49.49014	-0.36838	1048	1	2	313	59	50	31	-	-	G049.4903-00.3694
49.48544	-0.37678	1048	-	-	313	59	2	6	1	6	G049.4885-00.3799, G049.4903-00.3694
49.48867	-0.38734	1050	9	7	326	61	51	32	10	20	G049.4885-00.3799
49.48973	-0.36881	1050	9	7	326	61	51	32	10	20	G049.4903-00.3694
49.48466	-0.37687	1050	-	-	326	61	4	9	-	-	G049.4885-00.3799, G049.4903-00.3694
49.48466	-0.37687	1050	-	-	326	61	2	6	-	-	G049.4885-00.3799, G049.4903-00.3694
49.48551	-0.36269	1050	-	-	-	-	-	-	1	6	G049.4883-00.3545A, G049.4883-00.3545B, G049.4903-00.3694
61.47805	0.09104	1061	-	-	2	4	-	-	-	-	G061.4736+00.0908A, G061.4736+00.0908B, G061.4736+00.0908C

Appendix C: Observation log

Table C.1. Observation log.

Field	RA hh:mm:ss	Dec dd:pp:ss	ℓ	b	Date	OD	Start	Nominal OBSID	Ortho. Start
290	11:05:14.266	-60:57:38.79	290.400	-0.700	2010-08-15	459	15:42:32	1342203081(+1)	18:21:52
292	11:22:31.063	-61:42:12.77	292.600	-0.629	2010-08-14	458	20:53:20	1342203065(-1)	18:01:48
294	11:40:34.588	-62:18:00.17	294.800	-0.552	2010-08-14	458	26:24:29	1342203067(-1)	23:32:57
297	11:59:16.713	-62:44:25.30	297.000	-0.471	2010-08-15	458	07:55:37	1342203069(-1)	05:04:05
299 ^a	12:18:26.910	-63:00:59.70	299.200	-0.384	2009-09-03	112	03:21:32	1342183075(+1)	06:26:26
301	12:37:52.625	-63:07:23.91	301.400	-0.292	2010-08-15	459	24:06:14	1342203084(-1)	21:14:42
303 ^b	12:57:20.191	-63:03:29.76	303.600	-0.194	2010-01-08	239	04:03:19	1342189081(+1)	07:15:22
305 ^b	13:16:35.719	-62:49:20.56	305.800	-0.091	2010-01-08	239	13:40:19	1342189084(-1)	10:27:43
308	13:35:27.781	-62:26:15.89	308.000	0.000	2010-08-16	459	05:38:17	1342203086(-1)	02:46:45
310	13:53:56.541	-61:59:11.46	310.200	0.000	2010-08-20	464	22:27:35	1342203279(-1)	19:36:03
312 ^b	14:11:47.708	-61:23:08.81	312.400	0.000	2010-01-09	240	04:06:20	1342189110(-1)	00:53:44
314	14:28:53.915	-60:38:41.13	314.600	0.000	2010-08-21	464	01:07:08	1342203280(+1)	03:46:28
316	14:45:10.082	-59:46:25.81	316.800	0.000	2010-08-21	464	06:37:45	1342203282(+1)	09:17:05
319	15:00:33.335	-58:47:02.32	319.000	0.000	2010-08-21	465	17:57:13	1342203289(+1)	20:36:33
321	15:15:02.740	-57:41:10.22	321.200	0.000	2010-08-21	465	26:19:33	1342203292(-1)	23:28:01
323 ^b	15:28:38.841	-56:29:28.17	323.400	0.000	2010-01-29	261	24:48:03	1342189879(-1)	21:35:27
325	15:41:23.367	-55:12:32.49	325.600	0.000	2010-08-22	465	04:59:07	1342203293(+1)	07:38:27
327	15:53:18.797	-53:50:57.02	327.800	0.000	2010-09-03	478	24:11:19	1342204043(-1)	21:19:47
330	16:04:28.099	-52:25:12.66	330.000	0.000	2010-09-04	478	05:42:27	1342204045(-1)	02:50:55
332	16:14:54.520	-50:55:47.08	332.200	0.000	2010-09-04	478	08:21:47	1342204046(+1)	11:01:07
334	16:24:41.348	-49:23:05.26	334.400	0.000	2010-09-04	479	24:20:00	1342204055(-1)	21:28:28
336	16:33:51.865	-47:47:29.17	336.600	0.000	2010-09-05	479	05:51:08	1342204057(-1)	02:59:36
338	16:42:29.198	-46:09:18.44	338.800	0.000	2010-09-05	479	11:22:16	1342204059(-1)	08:30:44
341	16:50:36.309	-44:28:50.42	341.000	0.000	2010-09-06	480	13:55:21	1342204095(-1)	11:03:49
343	16:58:15.976	-42:46:20.19	343.200	0.000	2010-09-06	480	08:24:15	1342204093(-1)	05:32:43
345	17:05:30.743	-41:02:01.36	345.400	0.000	2010-09-06	480	02:53:09	1342204091(-1)	00:01:37
347	17:12:22.972	-39:16:05.62	347.600	0.000	2010-09-06	481	25:27:08	1342204101(-1)	22:35:36
349	17:18:54.803	-37:28:43.53	349.800	0.000	2011-02-20	647	07:34:31	1342214511(-1)	04:42:59
352	17:25:08.192	-35:40:04.45	352.000	0.000	2011-02-20	648	20:02:47	1342214576(-1)	17:11:15
354	17:31:04.932	-33:50:16.46	354.200	0.000	2011-02-24	651	04:29:59	1342214713(+1)	07:09:19
356	17:36:46.638	-31:59:27.04	356.400	0.000	2010-09-12	486	12:19:22	1342204369(-1)	09:27:50
358 ^c	17:42:14.801	-30:07:42.57	358.600	0.000	2010-09-12	486	06:48:07	1342204367(-1)	03:56:26
0 ^c	17:45:37.199	-28:56:10.23	0.000	0.000	2010-09-07	481	04:08:11	1342204102(+1)	06:47:44
2 ^c	17:50:46.049	-27:03:08.22	2.200	0.000	2010-09-07	481	09:39:03	1342204104(-1)	12:18:36
4	17:55:44.665	-25:09:25.47	4.400	0.000	2011-02-24	652	13:30:00	1342214761(+1)	16:09:20
6	18:00:34.119	-23:15:06.43	6.600	0.000	2011-02-24	652	19:01:17	1342214763(+1)	21:40:37
8	18:05:15.396	-21:20:15.19	8.800	0.000	2011-04-09	695	02:11:54	1342218963(+1)	04:51:14
11	18:09:49.409	-19:24:55.45	11.000	0.000	2011-04-09	695	07:43:15	1342218965(+1)	10:22:35
13	18:14:17.005	-17:29:10.63	13.200	0.000	2011-04-10	696	13:36:51	1342218999(+1)	16:16:11
15	18:18:38.972	-15:33:03.90	15.400	0.000	2011-04-10	696	10:57:27	1342218998(-1)	08:05:55
17	18:22:56.053	-13:36:38.19	17.600	0.000	2011-04-10	696	05:26:14	1342218996(-1)	02:34:42
19	18:27:08.946	-11:39:56.26	19.800	0.000	2011-04-15	701	09:54:54	1342218644(+1)	12:34:14
22	18:31:18.313	-9:43:00.72	22.000	0.000	2011-04-15	701	07:15:30	1342218643(-1)	04:23:58
24	18:35:24.790	-7:45:54.02	24.200	0.000	2011-04-15	701	15:26:36	1342218646(+1)	18:05:56
26	18:39:28.986	-5:48:38.52	26.400	0.000	2011-04-16	702	14:23:37	1342218696(+1)	17:02:57
28	18:43:31.490	-3:51:16.53	28.600	0.000	2011-04-16	702	08:52:59	1342218694(+1)	11:32:19
30 ^d	18:46:05.222	-2:36:32.90	30.000	0.000	2009-10-24	163	02:33:54	1342186275(+1)	05:39:08
30filler ^e	18:48:28.610	-1:09:31.80	31.563	+0.130	2011-10-24	893	09:38:00	1342231361(+1)	10:40:30

Notes. Column field gives the ID of each tile, the next four columns report the coordinates (equatorial and Galactic) of the centre of the tile, the date is the date of the observation (yyyy-mm-dd), OD is the *Herschel* operational day (with OD 1 corresponding to 14 May 2009), start is the start time (hh:mm:ss): if the second observation was begun after midnight, the start time is increased by 24 h, OBSID is the *Herschel* identifier of the observation: the OBSID for the orthogonal scan is +1 or -1, according to the value given in parenthesis. Unless stated differently, all the maps have a size of $2^\circ \times 2^\circ$ and the observations lasted 9490 s and 10 189 s for the two scans. ^(a) Observed during the performance verification phase: duration was 10930 s for both scans; ^(b) duration was 11453 s for both scans; ^(c) duration was 9499 s and 10198 s for the two scans. SPIRE was used in bright-source mode; ^(d) observed during the science demonstration phase: duration was 10940 s for both scans; ^(e) size is 120×35 arcmin², duration was 3662 s and 5599 s for the two scans; ^(f) size is 130×30 arcmin², duration was 3654 s and 5717 s for the two scans.

Table C.1. continued.

Field	RA hh:mm:ss	Dec dd:pp:ss	ℓ	b	Date	OD	Start	Nominal OBSID	Ortho. Start
33	18:51:33.726	+0:03:38.13	33.000	0.000	2011-04-16	702	06:13:19	1342218693(-1)	03:21:47
35	18:55:34.588	+2:01:06.44	35.200	0.000	2011-04-26	712	16:39:59	1342219631(-1)	13:48:27
37	18:59:36.031	+3:58:32.52	37.400	0.000	2010-10-23	528	24:48:50	1342207027(-1)	21:57:18
39	19:03:38.623	+5:55:54.18	39.600	0.000	2010-10-24	528	06:19:59	1342207029(-1)	03:28:27
41	19:07:42.942	+7:53:09.18	41.800	0.000	2010-10-24	528	11:51:08	1342207031(-1)	08:59:36
44	19:11:49.580	+9:50:15.27	44.000	0.000	2010-10-24	529	26:42:28	1342207053(-1)	23:50:56
46	19:15:59.148	+11:47:10.05	46.200	0.000	2010-10-25	529	08:13:37	1342207055(-1)	05:22:05
48	19:20:12.280	+13:43:51.05	48.400	0.000	2011-11-05	905	06:33:30	1342231859(-1)	03:41:58
50	19:24:29.643	+15:40:15.66	50.600	0.000	2011-11-04	904	08:55:34	1342231851(+1)	11:34:54
52	19:28:32.384	+17:38:53.32	52.800	+0.088	2011-10-23	892	10:22:02	1342231342(-1)	07:30:30
55	19:32:35.799	+19:37:48.65	55.000	+0.198	2011-05-02	718	13:13:23	1342219813(-1)	10:21:51
57	19:36:46.510	+21:36:13.38	57.200	+0.301	2011-05-02	718	18:44:29	1342219815(-1)	15:52:57
59 ^d	19:41:44.297	+23:01:21.60	59.000	0.000	2009-10-23	162	10:28:59	1342186235(+1)	13:34:13
59filler ^f	19:44:00.000	+24:10:00.00	60.250	+0.119	2011-11-05	905	09:14:34	1342231860(+1)	10:16:38
61	19:45:33.109	+25:31:19.18	61.600	+0.492	2011-05-03	719	15:17:59	1342220536(-1)	12:26:27
63	19:50:10.833	+27:27:53.52	63.800	+0.579	2011-10-23	892	04:49:22	1342231340(-1)	01:57:50
66	19:54:59.545	+29:23:43.65	66.000	+0.661	2011-10-22	892	23:18:16	1342231338(-1)	20:26:44